Diploma Thesis

# On the Reversibility of Dislocation Pile-ups at the Micron Scale: A $\mu$Laue Diffraction Study

Marlene Kapp


Department Materials Physics at the
University of Leoben

# Affidavit

I declare in lieu of oath, that I wrote this thesis
and performed the associated research myself,
using only literature cited in this volume.

Date

Signature

# Abstract

Microbending tests on single crystalline and bicrystalline copper bending beams were performed to contribute to a further understanding of dislocation plasticity on the micron scale. The in situ $\mu$Laue technique was used to investigate the origin of the non-ideal elastic unloading behavior due to a plastic reverse deformation during unloading. Additional in situ scanning electron microscopy (SEM) experiments were performed using a Hysitron PicoIndenter with a high force resolution. Bending beams with three different conditions at the neutral axis were used. The first sample type was a single crystalline bending beam revealing plastic reverse deformation during unloading. The driving force for this reverse deformation is a backstress induced by a dislocation pile-up built during plastic deformation. The backstress causes the dissolution of the dislocation pile-up during unloading leading to the plastic reverse deformation. The $\mu$Laue data confirm the partial reduction of the geometrically necessary dislocation density during unloading, proving the dissolution of the dislocation pile-up. The second sample type was a bicrystalline bending beam, with the grain boundary aligned along the neutral axis. Contrary to the $\mu$Laue data, the SEM experiments showed an amplified plastic reverse deformation during unloading compared to the single crystalline bending beam. This is due to the strict confinement of the pile-up at the boundary, causing a higher backstress and a stronger dissolution of the dislocation pile-up. The third sample type was a single crystalline bending beam, where the neutral axis was removed. During loading a major amount of dislocations could escape to the inner bending beam surface. Consequently, only a small dislocation pile-up and backstress were formed, leading to an almost ideal elastic unloading behavior.

# Acknowledgements

I would like to thank Dr. Gerhard Dehm for the possibility to write a diploma thesis and for his nice and patient supporting. Special thanks go to Dr. Christoph Kirchlechner for the numerous assistance, discussions and for his claimed time.

I would like to particularly mention Gabriele Moser and DI Wolfgang Liegl, who helped me with the sample preparation and encouraged me in all phases I worked on this thesis. I also want to thank Dr. Christian Motz and Dr. Anton Hohenwarter for enlightening discussions. Further thanks go to my nice colleagues from the office and to all my friends at the Erich-Schmid-Institut.

To Leoben you do not only come for studying, but also for making friends. I would like to thank those people who shared the years of study.

Great thanks go to my boyfriend Oliver Renk, who supported me all over the years and showed me that learning is not everything. Finally, I am grateful to have such great parents and sisters. The backing of my family made everything possible and easier.

# Contents

# Chapter 1

# Introduction

The development towards the miniaturisation of components such as devices for the microelectronic industry or for medical devices requires a thorough understanding of material behavior in the micro- and submicrometer regime. Therefore micromechanical tests under compression, tension, bending or monotonic cycling loading conditions are carried out to determine the material properties in this length scale. The achieved insights are not only fundamental for the construction of devices but also to attain an enhanced life time of components.

Several publications deal with the tensile [1, 2] or compression behavior [3, 4] of samples at the micron scale. Microbending experiments were done as well [5–8], even though the strain and stress gradient along the cross section of the bending beam hinders a simple evaluation and interpretation of the mechanical data.

A particular characteristic observed in microbending tests is a reverse deformation during unloading leading to a nonlinear unloading curve, as shown by Motz et al. [6], Demir et al. [7] or Gong et al. [8]. This plastic recovery is due to a reverse motion of dislocations during unloading, which is attributed to the Bauschinger effect according to Demir [7]. Several efforts were made to clarify the nature of this behavior, applying *in situ* bending experiments [6–8] or 3D-Discrete Dislocation Dynamics (3D-DDD) simulations [9]. In the present work further insights should be provided using the *in situ* $\mu$Laue technique. The scope is to interlink the nonlinearity of unloading curves with dislocation activity in bending experiments.

In 1886 Bauschinger predicted a back deformation at stress levels below the materials flow stress upon load reversal [10]. This phenomenon was later named Bauschinger effect.

Hasegawa [11] described the origin of the Bauschinger effect for aluminum single crystalline samples, in terms of dislocation cell walls hindering free dislocation motion. This leads to the formation of dislocation pile-ups causing a backstress with reversed sign of the applied load, affecting the following dislocations. During unloading and in the early stage of reverse loading the pile-up becomes smaller due to a back flow of piled up dislocations, leading to a reduction of plastic strain (Bauschinger strain). In a later stage of reverse loading also dislocations from the built cell walls are released, contributing to the applied deformation.
Recently the effect of reverse deformation was investigated in loading-unloading experiments on ultrafine-grained tension samples by Mompiou [12]. A nonlinear unloading curve as shown in figure 1.1 was revealed. The authors could explain the pronounced nonlinearity of the unloading curve of the ultrafine-grained samples by doing *in situ* TEM. They found a pile-up of dislocations at the grain boundaries when cross-slip of dislocations in the pile-up was suppressed. Thus, it is evident that a reverse deformation upon unloading occurs in the case that dislocation glide is hindered during loading, leading to a dislocation pile-up and a certain pile-up stress.

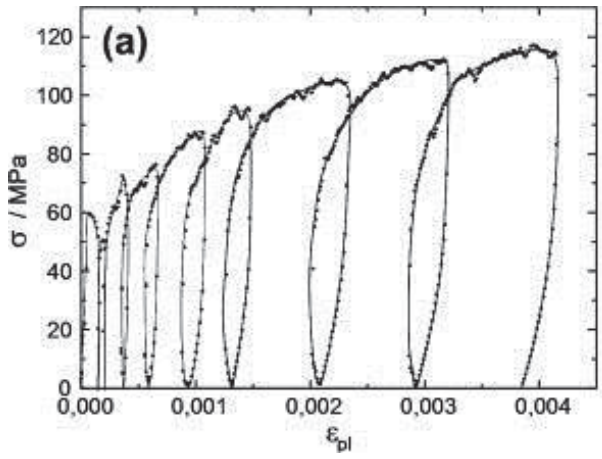


**Figure 1.1** Stress-strain-curve from loading-unloading experiments on ultrafine-grained aluminum tensile samples showing reverse deformation during unloading in terms of a nonlinear unloading curve reprinted from [13].

Another factor is the different deformation behavior of micronsized samples and their macroscopic counterparts. For example, the number of dislocation sources in a micron sized bending beam is limited and leads to a localized deformation on distinct glide planes. In contrast to the deformation of macroscopic samples, where a more uniform deformation

process occurs, the pile-up of dislocations in microscopic bending samples is expected to be more pronounced. The higher pile-up stress leads to a higher backstress affecting the following dislocations in the pile-up and the dislocation source.
In recent studies a nonlinear unloading curve was depicted in microbending tests [6, 7, 14]. In 3-D DDD simulations from Motz [9] using micronsized copper bending beams a pile-up at the neutral axis was generated during loading. The plastic back deformation during unloading was attributed to a pile-up of geometrically necessary dislocations (GNDs) at the neutral axis of the bending beam as illustrated in figure 1.2 [6]. Because of the low stacking fault energy a cross slip of the piled up dislocations in order to avoid the pile-up stresses is prevented and they remain in the pile-up during loading. In case of unloading or load reversal the dislocations partly leave the sample as a consequence of the induced backstress and dislocation pile-ups are reversible removed or at least reduced. This process results in a back flow during unloading leading to a nonlinear unloading curve.

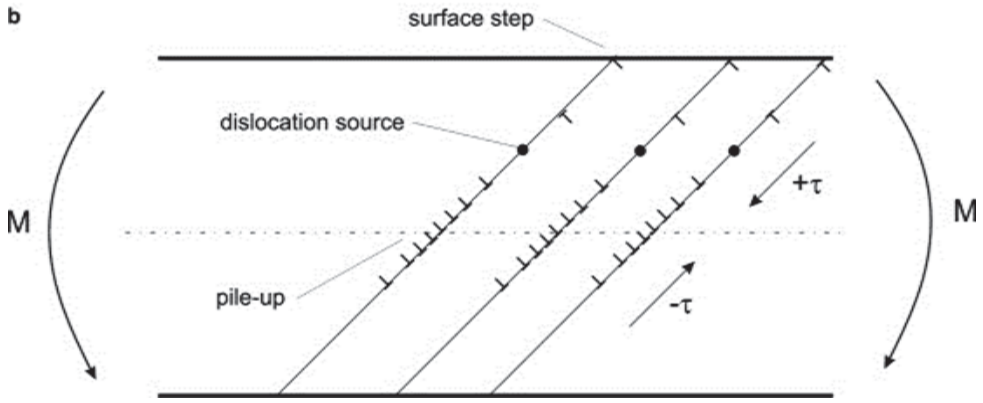


**Figure 1.2** Pile-up of dislocations at the neutral axis of a bending beam with an applied bending moment M and the shear stress $\tau$ acting on the slip plane reprinted from [6].

The challenge is to find an appropriate procedure to quantify the amount of plastic reverse deformation in microscopic dimensions. A well suited tool for analyzing the formation of dislocation structures is the $\mu$Laue technique. Concerning the deformation behavior in microscopic dimensions promising results were achieved with *ex situ* [15] and *in situ* $\mu$Laue measurements on compression [16, 17], tension [18] as well as bending [14] samples. Additionally it is an appropriate method to quantify the amount of plastic reverse deformation, especially in the reverse flow of GNDs, as it is sensitive to the number, the type and the arrangement of GNDs [19–21]. More detailed information is given in chapter 2.2. The

experiments conducted in this thesis are *in situ* $\mu$Laue bending experiments at the ESRF in Grenoble at the french beamline BM32 CRG-IF as well as *in situ* SEM bending experiments with a Hysitron PicoIndenter PI 85 at the Erich-Schmid-Institut in Leoben. The *in situ* $\mu$Laue experiments serve to interlink the mechanical data with the evolution of the dislocation structure, in particular with the GND density. Furthermore the number of GNDs annihilated at the sample surface or redistributed in the sample volume can be depicted. The excellent force resolution of the Hysitron indenter enables accurate stress-strain curves.

Three bending beam geometries (Fig. 2.2) exhibiting different boundaries at the neutral axis (Fig. 1.3) were tested in bending experiments with several loading and unloading steps.

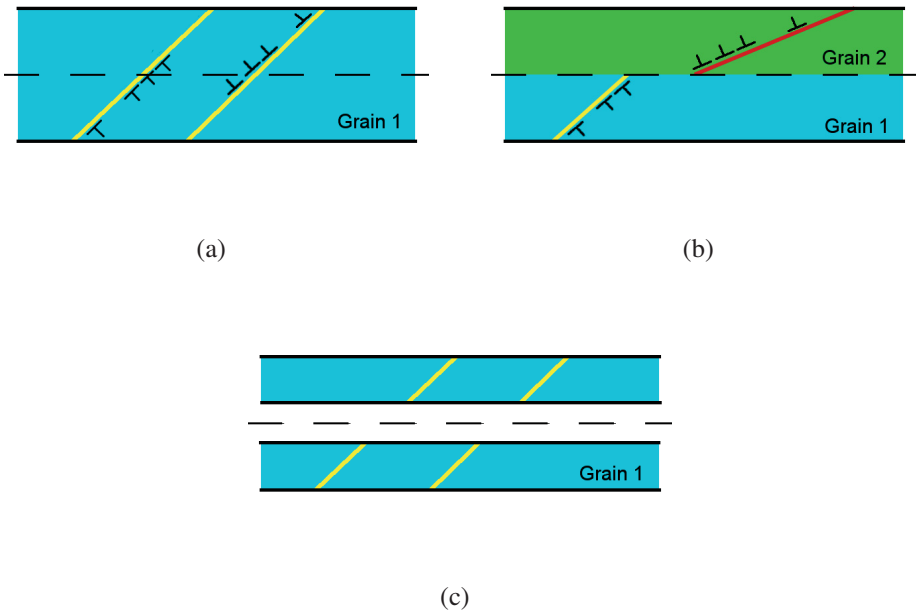


(a) (b)

(c)

**Figure 1.3** Illustration of the different bending beam geometries used in this study: a) single crystalline bending beam with slip plane (yellow) and dislocation pile-ups near the neutral axes (detail from Fig. 2.2a), b) bicrystalline bending beam with slip plane of grain one (yellow) and grain two (red), as well as dislocation pile-ups at the grain boundary, equal position as neutral axis, (detail from Fig. 2.2b), c) bending beam with slit along the neutral axis, here no boundary exists (detail from Fig. 2.2c).

The first sample type is a single crystalline bending beam (Fig. 1.3a). As recently published by Kirchlechner et al. [14] the unloading curve is not ideal elastic for this sample type and shows

a reversible plastic back deformation (Fig. 1.4 in green). Based on this work two further types of sample geometries are used to amplify (type two) and accordingly weaken (type three) the reversible plastic back deformation. Therefore the second sample type is a bicrystalline bending beam, where the neutral axis is accompanied by a grain boundary (Fig. 1.3b). The grain boundary is expected to be a stronger, impenetrable barrier for the dislocations resulting in a more pronounced dislocation pile-up and a greater degree of plastic back deformation (Fig. 1.4 in light blue). As the neutral axis of the third sample type is cut out, a pile-up of GNDs is not possible or at least reduced. The unloading curve is expected to be elastic and a reversible plastic back deformation should not appear (Fig. 1.4 in dark blue).

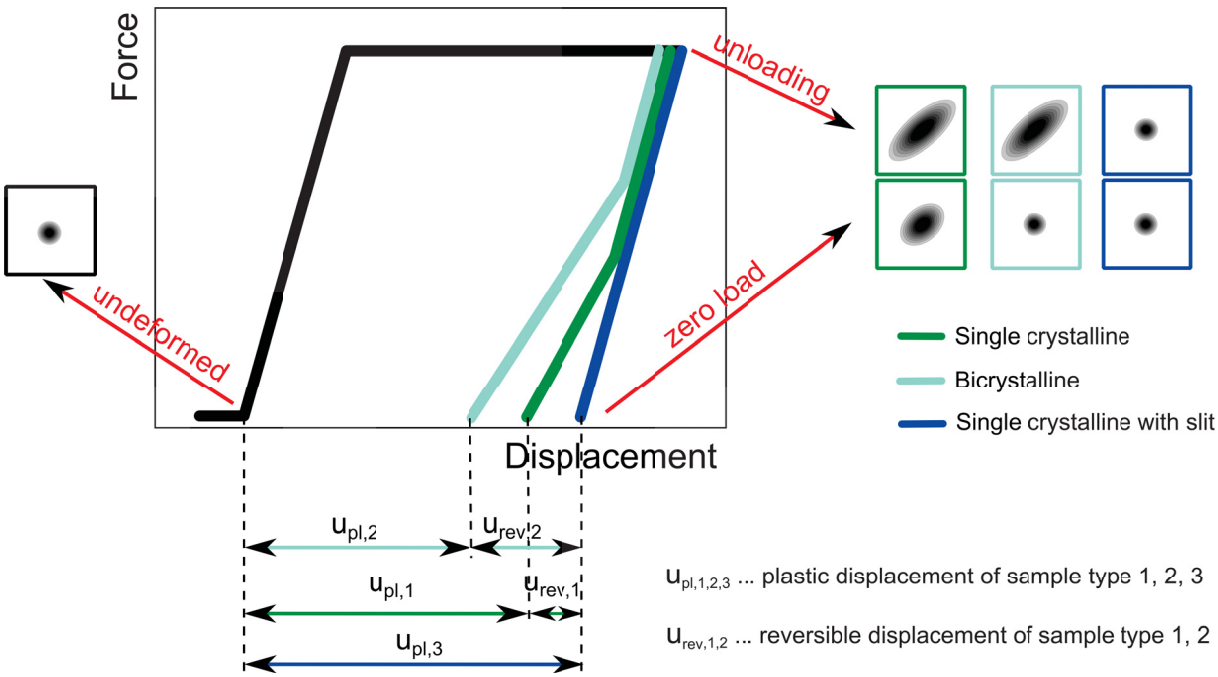


**Figure 1.4** Schematic force-displacement curves and corresponding Laue spots of the single crystalline sample (green), the bicrystalline sample (light blue) and the single crystalline sample with the slit being orientated along the neutral axis (dark blue).

$\mu$Laue patterns of perfect strain free single crystals are characterized by circular, symmetric peaks as illustrated in figure 1.5. The peak shape is changing with deformation: In case of statistically stored dislocation (SSDs) a symmetric broadening of the peaks occurs, whereas GNDs lead to an elongation, the so called streaking, of the peaks. For the investigation of the reverse flow of GNDs the change in the peak shape from the point of unloading to the point of zero load is of major interest. As already shown in [14] the single crystalline sample exhibits a

reduction of the Laue peak streaking after unloading (Fig. 1.4, green frame). This is attributed to GNDs leaving the bending beam within the illuminated volume due to the backstress induced by the dislocation pile-up at the neutral axis. As an increase of the backstress due to the restrictions caused by the boundary is expected for the bicrystalline sample, the peak streaking should be reduced after unloading until the peak shape approaches its initial state (Fig. 1.4, light blue frame). As most of the dislocations in the single crystalline sample with the slit along the neutral axis can leave the sample and form slip steps, the peak streaking at the point of unloading is weaker. Due to the missing or less pronounced dislocation pile-up the peak shape should not change during unloading (Fig. 1.4, dark blue frame).

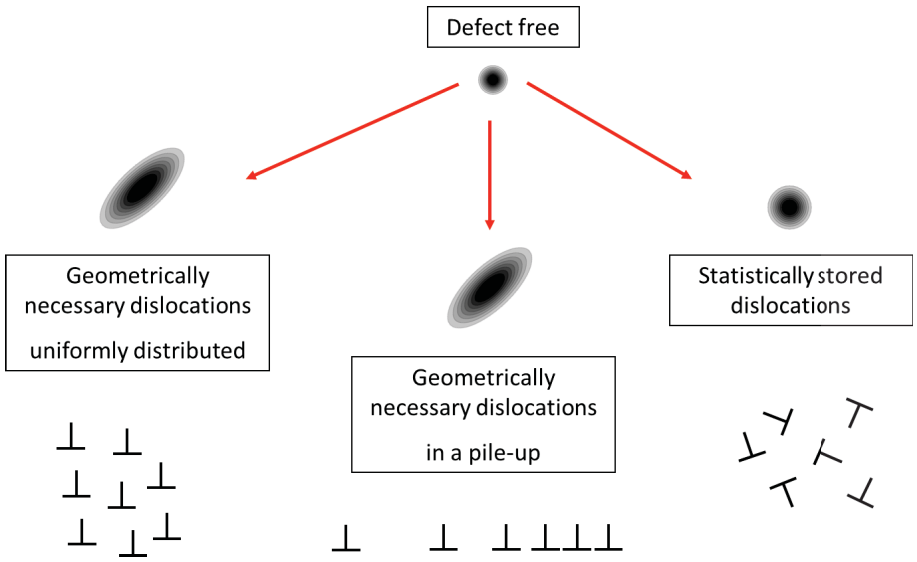


**Figure 1.5** Evolution of the initial circular peak shape due to bending: broadened circular peak shape if statistically stored dislocations are generated, streaked peak shape if GNDs are generated.

# Chapter 2

# Experimental Methodology

## 2.1 Sample Preparation

### 2.1.1 Macroscopic Samples

The macroscopic samples were prepared following the approach of Moser et al. [22] as illustrated in figure 2.1. The macro-samples should have a small thickness for a reduced FIB milling time. Therefore a 1 mm thick slice was cut from a Copper bicrystal provided by Dr. Zhang of the Shenyang National Laboratory for Materials Sciences, Institute of Metal Research of the Chinese Academy of Sciences. The slice was subsequently cut with a diamond wire saw into three 10x3 $mm^2$ disks (Fig. 2.1a). These disks were thinned to a thickness of 180 $\mu$m using a grinding paper with a grain size of 15 $\mu$m (Fig. 2.1b). A lacquer resisting the electrolyte was brushed onto the platelets, missing one edge where they should be thinned afterwards (Fig. 2.1c). Electrochemical etching to a final wedge thickness of 20 $\mu$m was performed using the commercial electrolyte D2 provided by Struers GmbH (Willich/Germany) applying 2V DC (Fig. 2.1d). Finally the lacquer was removed with Aceton and the platelets were fixed onto sample holders (Fig. 2.1e).

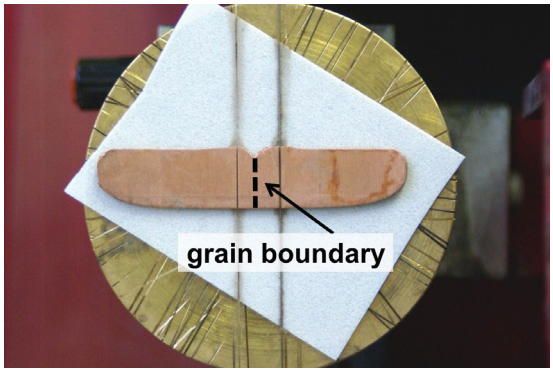


(a)

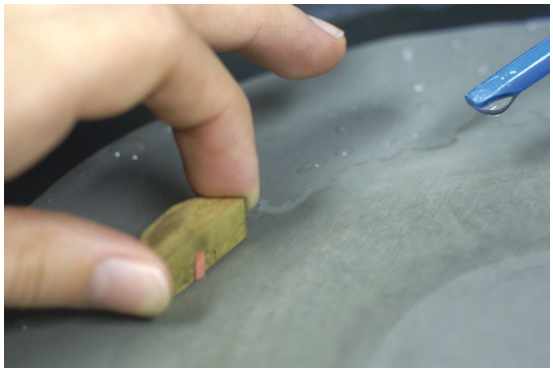

(b)

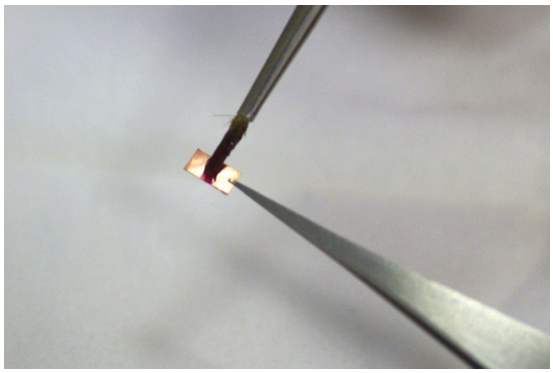

(c)

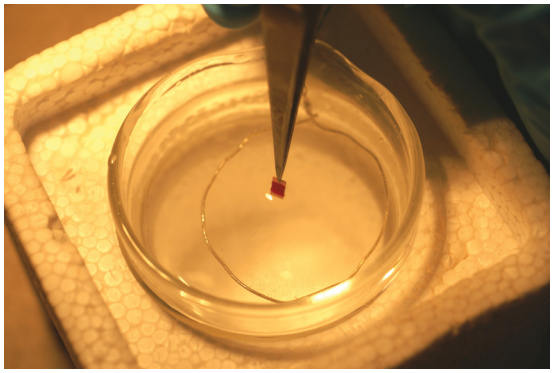

(d)

(e)

**Figure 2.1** Stages of macroscopic sample preparation: a) Cutting with a diamond wire saw, b) grinding of the disks, c) lacquer brushed next to the sample area, d) electrochemical etching of the sample area, e) final sample glued on the sample holder.

### 2.1.2 Microscopic Samples

#### Sample Geometry

The microscopic samples were produced by focused ion beam (FIB) milling. Thereby a Gallium ion beam sputters surface atoms away from a defined sample area. A variety of sample geometries can be realized in that way, which is described in more detail in [23] and [24]. The bending beams were manufactured with a ZEISS 1540 XB FIB workstation, which is a crossbeam workstation consisting of an ion column and an electron column. The FIB milling was done by an acceleration voltage of 30 keV using a coarse milling current of 10 nA and a polishing current of 500 pA for the final bending beam surface. Three different types of bending beam geometries were manufactured:

- Single crystalline bending beam (Fig. 2.2a)
- Bicrystalline bending beam with the grain boundary along the neutral axis (Fig. 2.2b)
- Single crystalline bending beam with a slit cut out along the neutral axis (Fig. 2.2c)

#### Sample Orientation

The expected nominal orientation of grain 1 in the single crystalline (Fig. 2.2a), bicrystalline (Fig. 2.2b) and the single crystalline bending beams with the slit (Fig. 2.2c) was a single slip [234] crystal direction as shown in figure 2.2a. In fact, Laue measurements revealed for grain 1 a multiple slip $[02\overline{1}]$ crystal direction corresponding with the bending beam axis as exemplarily shown for sample A5 (Fig. 2.3). The misorientation between grain 1 and grain 2 in the bicrystalline bending beams is 24°. The orientations from other samples are provided by inverse pole figures in chapter 4.

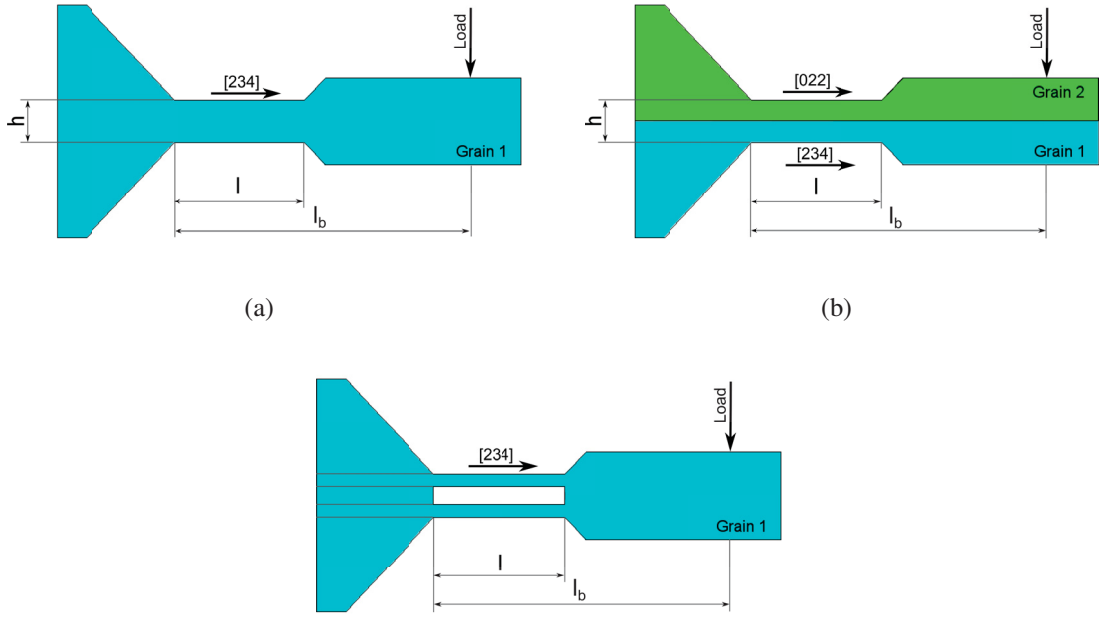


**Figure 2.2** Schematic drawing of the used bending beam geometries with the length $l$, the height $h$, the height of the slit $h_{slit}$ and the bending length $l_{bend}$: a) single crystalline bending beam, b) bicrystalline bending beam, c) bending beam with slit along neutral axis. The nominal [234] crystal direction of grain 1 and [022] crystal direction of grain 2 corresponding with the bending beam axis, are marked by black arrows. The dimensions of the FIB structured samples are listed in section 2.2.3.

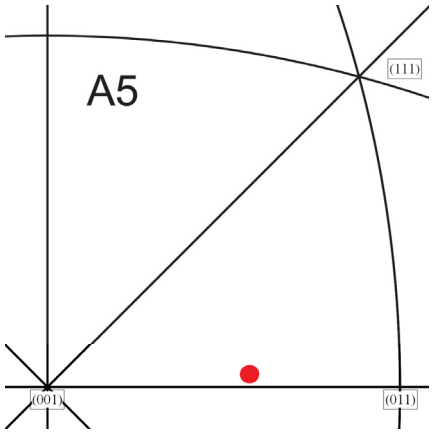


**Figure 2.3** The $[02\bar{1}]$ crystal direction corresponding with the bending beam axis of the single crystalline sample A5 (red dot) is close to a multiple slip orientation, with the red dot nearly lying on the connecting line between the corner orientations (001) and (011).

## 2.2 $\mu$Laue Diffraction

### 2.2.1 Basics of Diffraction

Laue diffraction has been known for over a hundred years now, since Max von Laue figured out that crystal lattice constants in the range of $10^{-11}$ m are well suited to cause interferences of X-rays with wavelengths in the range of $10^{-12}$ m [25]. Over the last decades the use of Laue diffraction has experienced further developments as there were enhancements on the generation of ultra-brilliant synchrotron radiation and X-ray beam focusing mirrors. The thereby achieved outstanding spatial and angular resolution with beam diameters in the submicrometer regime makes $\mu$Laue to a very powerful tool in material science since micron sized samples and single grains out of a polycrystalline microstructure can be tested [21].
From Bragg's law it is known that constructive interference only takes place under certain conditions (Eq. 2.1). The optical path difference between the two electromagnetic waves is dependent on the geometrical relationship of the spacing between the reflecting lattice planes $d_{hkl}$ and the angle $\Theta$ (Bragg angle) between the incident beam and the lattice plane (Fig. 2.4). In case of constructive interference the optical path difference has to be an integer multiple $n$ of the wavelength $\lambda$ [26].

$$2 \cdot d \cdot \sin\Theta = n \cdot \lambda \tag{2.1}$$

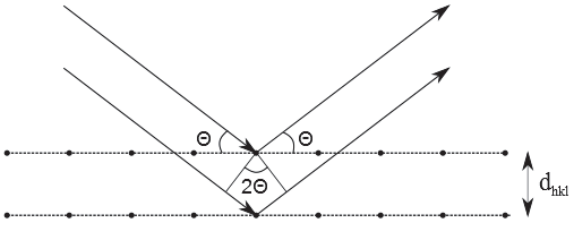


**Figure 2.4** Bragg's law with Bragg angle $\Theta$ and the lattice plane spacing $d_{hkl}$.

An alternative way to describe the conditions for diffraction according to Bragg's law is given by the Ewald sphere construction (Fig. 2.5). In the monochromatic case the radius of the Ewald sphere is given by the wave vector $\overline{k}_0$ of the incident X-ray beam, which is inverse proportional to its wavelength $\lambda$. Constructive interference occurs if the momentum transfer $\Delta\overline{k}$ = $\overline{k}$ - $\overline{k}_0$ from the wave vector of the incident ray $\overline{k}_0$ to the scattered one $\overline{k}$ intersects

a reciprocal lattice point, which is fulfilled for reciprocal lattice points being on the Ewald sphere. Hence, for single crystals probed with monochromatic X-rays the probability for constructive interference is small [20, 21, 26].
Polychromatic X-rays lead to a greater chance of reflection as the Ewald sphere is extended to a certain volume defined by the difference of the maximum wave vector $\overline{k}_{max}$ and the minimum one $\overline{k}_{min}$. If so, constructive interference occurs when the momentum transfer $\Delta\overline{k}$ intersects a reciprocal lattice point within the defined volume [20, 21, 26].

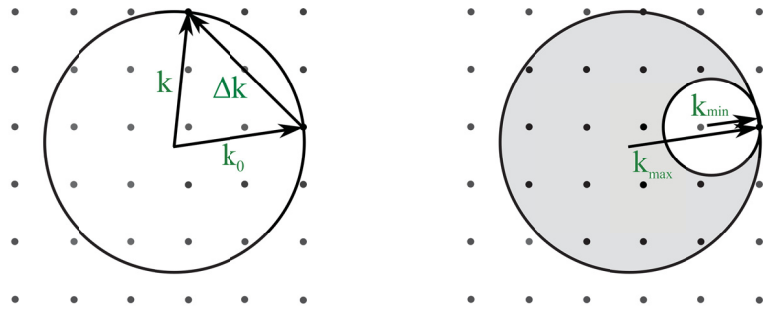


(a) (b)

**Figure 2.5** Ewald sphere construction for a) a monochromatic X-ray beam with reciprocal lattice points, incident wave vector $\overline{k}_0$, scattered wave vector $\overline{k}$ and the momentum transfer vector $\Delta\overline{k}$ and for b) a polychromatic X-ray beam with the maximum $\overline{k}_{max}$ and minimum wave vector $\overline{k}_{min}$ of the incident X-ray beam.

For $\mu$Laue experiments a white X-ray beam from synchrotron radiation with a broad energy band pass is used. Thus, multiple Laue spots are achieved simultaneously. It has the advantage that sample rotation is not required and consequently the illuminated volume is not changed continuously during the measurement [17]. Another benefit is the reduced measuring time.
Conventional Laue experiments are limited to single crystalline samples or at least samples with less than ten grains [27]. With more than ten grains, the number of Laue spots increases in such a way, that the indexation process becomes time consuming. Additionally it is difficult to assign the single spots to the according grains, if the number of grains is too high [17]. $\mu$Laue diffraction can overcome this limitation as it uses a micron sized beam diameter and thus can probe individual grains.

### 2.2.2 Sensitivity to Dislocations

The $\mu$Laue diffraction pattern of an unstrained sample with a perfect lattice (Fig. 2.6a) shows sharp spots (Fig. 2.7a) with distinct spacings in between. $\mu$Laue is sensitive to the number, the type (e.g. SSDs or GNDs) and the arrangement (e.g. subgrain boundaries) of dislocations in the sample volume, which results in an broadening of the sharp spot shape [20].

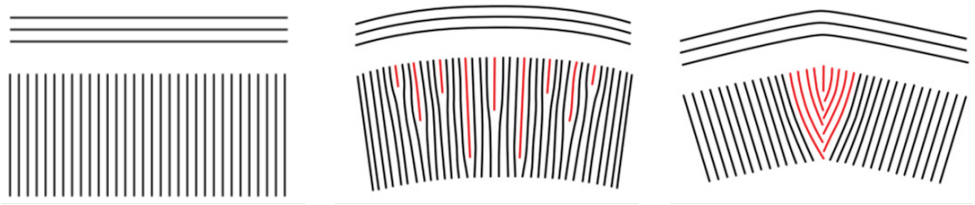

(a) (b) (c)

**Figure 2.6** Scheme of a) a perfect lattice without a lattice curvature, b) a lattice with GDNs leading to a lattice curvature, c) a lattice with a subgrain boundary. Reprinted with permission from [27].

The average net Burgers vector of SSDs $\bar{b}_{SSD}$ equals zero. These dislocations cause localized lattice curvatures which are canceled out over the averaged volume. If the density of SSDs is increased the intensity distribution around a Laue spot is symmetrical but can be broadened compared to the sharp spot of the unstrained sample [20].

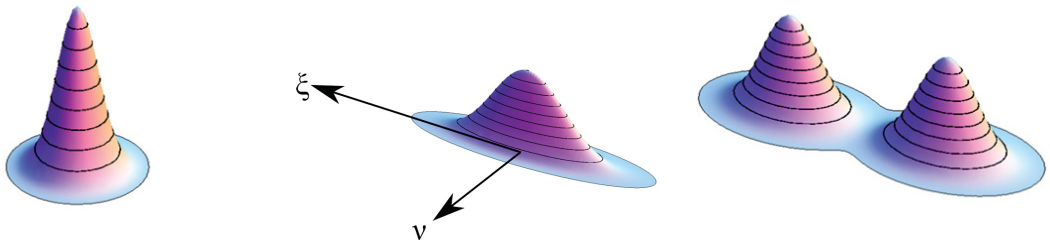


(a) (b) (c)

**Figure 2.7** Shape of Laue spots of a) a perfect lattice, b) a lattice with GNDs with the streaking direction $\xi$ and the perpendicular direction $\nu$ and c) two subgrains with a subgrain-boundary in between. Reprinted with permission from [27].

GNDs are generated to sustain a strain gradient as it is observed under an indent or in a bending beam. Their Burgers vectors share the same direction leading to a net Burgers vector $\overline{b}_{GND}$ unequal zero. The accumulation of GNDs results in a lattice curvature $\kappa$ (Fig. 2.6b), which can be interlinked to the density of dislocations $\rho$ as demonstrated in [28]. The curvature of the diffracting lattice planes leads to an elongation - the so called streaking - of the Laue spot (Fig. 2.7b) with $\xi$ marking the direction of streaking and $\nu$ the direction perpendicular to it. Thereby it is assumed that the contribution of elastic strains to the lattice curvature can be neglected [14]. The increase in the density of GNDs leads to a pronounced streaking of the Laue spot, which can be quantified by the Full Width at Half Maximum in streaking direction $\mathrm{FWHM}_{\xi}$ as shown in [27].
Dislocations can rearrange and form subgrain boundaries (Fig. 2.6c) in order to reduce the elastic strain energies [29]. This behavior results in a splitting of the Laue spot as illustrated in figure 2.7c [20, 27].

### 2.2.3 The $\mu$Laue Diffraction Set-up at the ESRF

The ESRF BM 32 bending magnet synchrotron source was used for the $\mu$Laue measurements. The pink synchrotron beam had an energy bandpass ranging from 5-25 keV [14] and was generated by a bending magnet, which is described more precisely in [26] and [30]. Subsequently the synchrotron beam was shaped to a final diameter of approximately 0.9 $\mu$m horizontally and 1.1 $\mu$m vertically by two pairs of slits and Kirkpatrick-Baez mirrors [31].

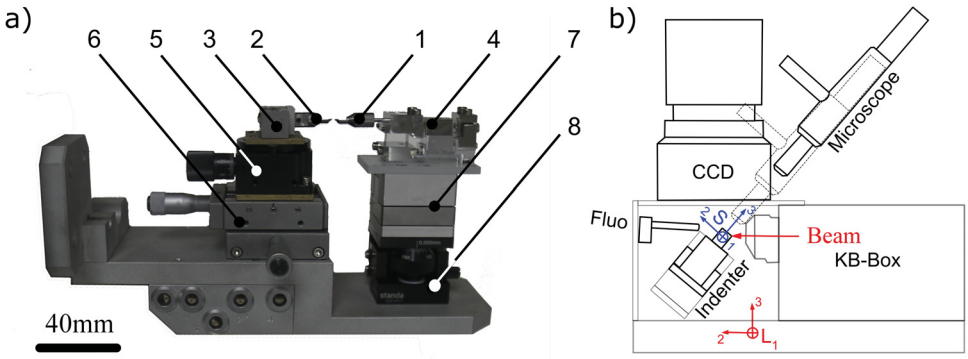


**Figure 2.8** a) Straining device: 1) sample, 2) counterbody, 3) piezos, 4) load cell, 5) rotation stage, 6-8) translation stage. b) Set-up of instrumental equipment at BM 32 with the optics (KB-Box), optical microscope, fluorescence detector, straining device (indenter) and CCD reprinted from [17].

The *in situ* test was performed as describe in [17] similar to [14, 16, 18]. The set-up of the instrumental equipment is given in figure 2.8 from [17]. The sample and the counterbody are roughly positioned using an optical microscope. A fluorescence detector serves for a precise alignment of the x-, y-position of the sample with respect to the synchrotron beam. The Laue patterns are recorded by a charge-coupled device (CCD, MAR165) with a readout time of approximately two seconds and a distance of 70 mm from the sample. At the beginning of the experiments a calibration is required, which is done by a germanium single crystal. For the *in situ* bending measurements a displacement controlled straining device was used (Fig. 2.8a) as presented in [17]. Thereby the sample is mounted on a stage, using piezos (PU-100) provided by piezosystems Jena. The counterbody is assembled on an opposite stage, where a coarse adjustment of the x-, y- and the rotation axis can be done manually using micrometer screws. The force is measured by a commercial load cell (Kammrath&Weiss) using the eigenfrequency of a tungsten wire with an accuracy of 10 $\mu$N. The whole straining device is mounted on a base frame on the moveable goniometer stage. The X-ray beam probes the sample area under an incidence angle of 40° perpendicular to the loading direction (Fig. 2.9 from [14]). Because of a redirected air flow of the air conditioning system, the load cell during measurements of sample B1 was affected. Consequently, the whole set-up was shielded from the air flow for the other samples. See chapter 6.5 for details .

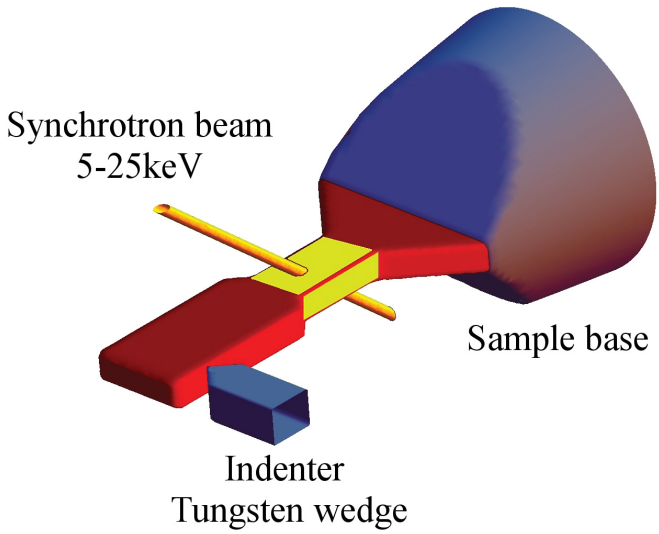


**Figure 2.9** Bending beam probed by the synchrotron beam under an incident angle of 40° reprinted from [14].

For the *in situ* $\mu$Laue experiments five samples from sample type 1 (single crystalline), three samples from sample type 2 (bicrystalline) and another three samples from sample type 3 (single crystalline with slit along neutral axis) were measured. The dimensions of the samples are given in table 2.1. Before and after the $\mu$Laue experiments SEM images were taken from each bending beam (Chp. 3.1). The bending experiments are performed in several loading and unloading steps 3.2. During each loading and unloading step the evolution of the Laue pattern is recorded with time. This experiment serves to detect the evolution of dislocation pile-ups at a position on the neutral axis of the bending beam while loading and unloading (Chp. 3.3). The calculation of the $\text{FWHM}_\xi$ and $\text{FWHM}_\nu$ was done on the base of a Mathematica routine provided by Dr. C. Kirchlechner. Before the experiment and after each second deformation step, a mesh scan with a step size of one or two microns was performed, revealing the evolution of the dislocation structure along the bending beam length and width (Chp. 3.4). An overview of the experiments performed with each sample are given in the appendix (Tab. 6.1).

| | **Sample** | **l [$\mu$m]** | **b [$\mu$m]** | **h [$\mu$m]** | **$\mathbf{h}_{slit}$ [$\mu$m]** | **$\mathbf{l}_{bend}$ [$\mu$m]** |
|---|---|---|---|---|---|---|
| **Sxx** | A1 | 19.87 | 6.03 | 5.55 | - | 28.66 |
| **Sxx** | A2 | 19.17 | 6.22 | 5.60 | - | 29.10 |
| **Sxx** | A3 | 21.55 | 6.66 | 6.59 | - | 38.04 |
| **Sxx** | A4 | 20.39 | 5.66 | 6.77 | - | 38.63 |
| **Sxx** | A5 | 21.12 | 7.15 | 7.28 | - | 46.26 |
| **Sxx** | A6 | 21.03 | 7.16 | 6.96 | - | 60.78 |
| **Bxx** | B1 | 20.54 | 6.03 | 6.07 | - | 31.69 |
| **Bxx** | B2 | 20.25 | 7.16 | 5.47 | - | 31.04 |
| **Bxx** | B3 | 20.47 | 7.25 | 6.89 | - | 36.10 |
| **Bxx** | B4 | 20.17 | 7.35 | 7.07 | - | 62.72 |
| **Slit** | C1 | 19.28 | 6.03 | 13.10 | 1.71 | 37.51 |
| **Slit** | C2 | 12.08 | 10.08 | 18.68 | 6.19 | 37.69 |
| **Slit** | C3 | 18.82 | 5.48 | 13.55 | 4.76 | 24.90 |
| **Slit** | C4 | 12.39 | 3.65 | 12.17 | 5.06 | 53.64 |

**Table 2.1** Sample dimensions of the single crystalline sample (A1-A6), the bicrystalline sample (B1-B4) and the single crystalline samples with the slit (C1-C4) tested with the $\mu$Laue method: $l$ is the length, $b$ is the width, $h$ is the height, $h_{slit}$ is the height of the slit, $l_{bend}$ is the bending length. These variables are defined in figures 2.2 and 2.12. Samples A6, B4, C4 were used for the *in situ* SEM measurements. The sample dimensions were measured in the SEM.

## 2.3 *In situ* Bending Tests with a Scanning Electron Microscope

Three different bending beam geometries were tested *in situ* with the Hysitron PicoIndenter PI 85 (Fig. 2.10) in a ZEISS 1540 XB FIB crossbeam workstation to prove the mechanical data from the $\mu$Laue experiments performed in Grenoble. Only one bending beam of each sample type was tested, with the sample dimensions given in table 2.1.
The sample was mounted on piezoactuators and could be moved towards the indenter with an accuracy in the nanometer regime. A boron-doped Berkovich indenter was attached to the opposite side on an immobile stage. Detailed information can be found in references [32, 33]. The samples were tested in a displacement controlled mode with a strain rate of $10^{-4}$ $s^{-1}$ to $10^{-5}$ $s^{-1}$. The force can be measured as precise as 0.1 $\mu$N with a three-plate transducer. Prior to the bending experiments, the PI 85 indenter was calibrated according to [34]. Indents for the correction of the residual indent depth were performed.

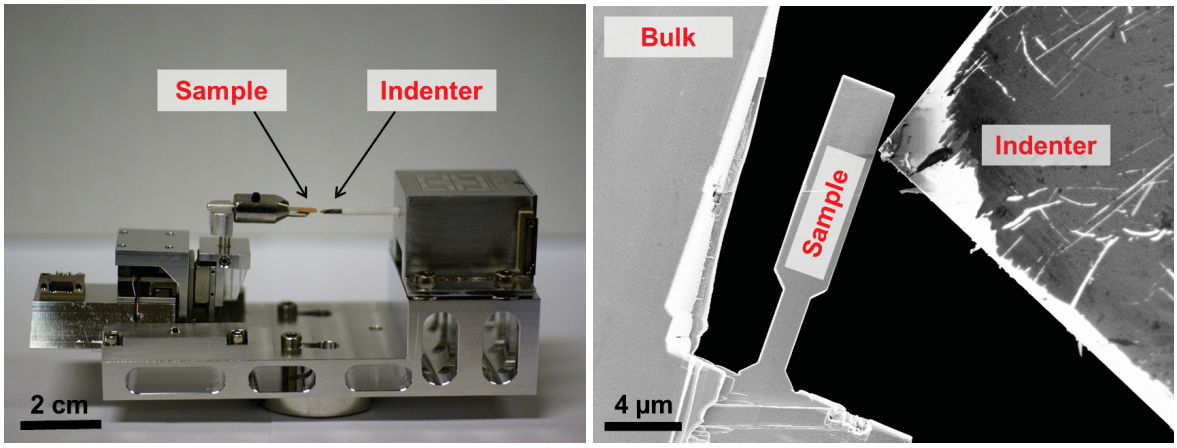


(a) (b)

**Figure 2.10** a) The set-up of the Hysitron PicoIndenter PI 85 with the indenter on the right and the macrosample on the left side. b) SEM image of the measuring set-up with the bending beam on the left and the Berkovich indenter on the right side.

## 2.4 Bending - Stress Distribution and Analysis

Considering the stress distribution of a bending beam tensile, compression and shear stresses exist, which are separated by the neutral axis in the middle of the cross section. The stress distribution is depending on the stage of loading.

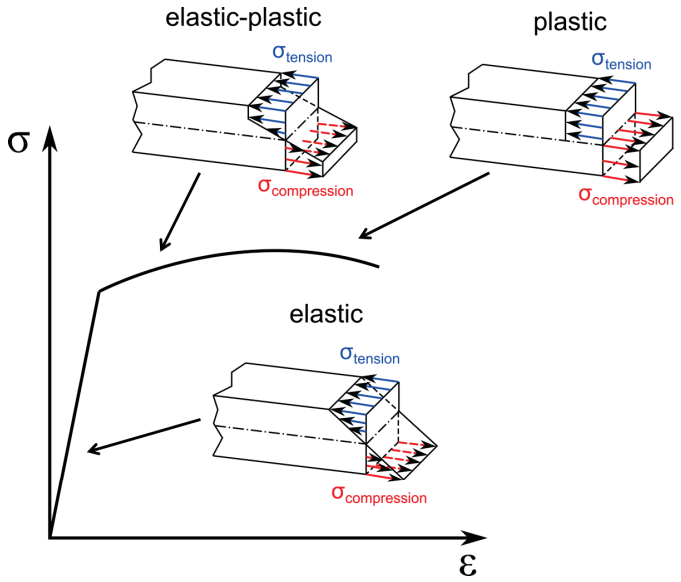


**Figure 2.11** Schematic stress distribution in a bending beam in the elastic, elastic-plastic and plastic loading regime.

In the elastic loading regime a linear stress gradient along the cross section of the sample exists, with the highest stresses appearing at the outer fiber (Fig. 2.11). The surface stress is calculated according to the linear elastic bending beam theory (Eq. 2.2), where $\sigma$ is the surface stress, $F$ is the Force, $l_b$ is the bending length, $b$ is the width and $h$ is the height of the bending beam:

$$\sigma = \frac{6 * F * l_b}{b * h^2} \tag{2.2}$$

In case of fully plastic loading conditions (Fig. 2.11) the tensile stresses are homogenously distributed over one half of the bending beam. The compression stresses are of the same magnitude but with reversed sign and homogenously distributed along the other half of the

bending beam. For fully plastic behavior the stress is evaluated according to equation 2.3:

$$\sigma = \frac{4 * F * l_b}{b * h^2} \tag{2.3}$$

In the elastic-plastic transition regime it is assumed that the material exhibits an elastic-plastic behavior (Fig. 2.11). This means that a homogenous plastic stress distribution for tensile and compression stresses occurs up to a certain distance from the outer fiber. Towards the center of the bending beam the behavior is elastic, revealing a stress gradient for tensile and compression stresses.

The difference between the linear elastic and plastic calculations is that the stress scales with a factor of 6 in the elastic and with a factor of 4 in the plastic case. However, equations 2.2 and 2.3 describe limiting cases. In fact there are always elastic and plastic contributions to the stress distribution as it is shown for the elastic-plastic transition regime in figure 2.11. This leads to a difficult interpretation of bending experiments.

Furthermore it has to be considered that the magnitude of the bending moment is changing with the bending length (Fig. 2.12). The maximum bending moment occurs at the clamping of the bending beam, which is decreasing towards the point of loading. In literature the evaluation of the normalized bending moment $M_{norm}$ according to equation 2.4 is quite common [35]:

$$M_{norm} = \frac{F * l_b}{b * h^2} \tag{2.4}$$

According to these considerations several ways are possible for the evaluation and interpretation of the mechanical data in a bending experiment. For simplicity, the mechanical data were analyzed by means of elastic bending beam theory (Eq. 2.2) in this work. The surface strain $\epsilon$ was calculated according to equation 2.5, where *e* stands for the distance of the neutral axis to the outer fiber, which is equal to $\frac{h}{2}$ in this case, *u* is the displacement of the indenter, *l* is the length of the sample gauge section:

$$\epsilon = \frac{e * u}{l_b * l} \tag{2.5}$$

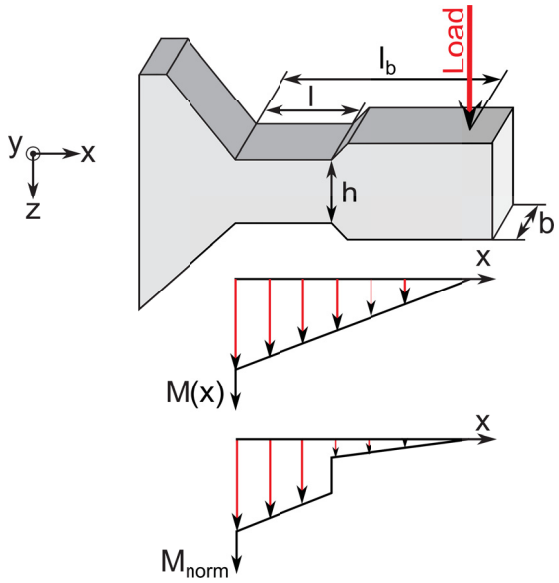


**Figure 2.12** Distribution of the bending moment M(x) = F*x along the bending length and the normalized bending moment $M_{norm}$ along the bending length from equation 2.4.

# Chapter 3

# Results

## 3.1 Glide Step Formation

The glide steps developed during the bending experiment were investigated by SEM images taken in a ZEISS dual beam workstation 1540 XB. In the following sections representative SEM pictures of all bending beam geometries are shown.

### 3.1.1 Type 1 - Single crystalline

Referring to figure 3.1a distinct glide steps occur in the tension (in the front) and compression side (in the back) of the bending beam. They are more pronounced towards the outer fiber of the bending beam and weaken towards the neutral axis. Additionally, the slip steps become stronger towards the left side, where the beam is fixed to the macrosample. Figure 3.1b reveals parallel slip traces on the compression and tension side of the bending beam. It has to be mentioned, that in sample number A5 (Fig. 6.1a in chapter 6) the slip steps are not parallel but of a different orientation in the compression and tension side.

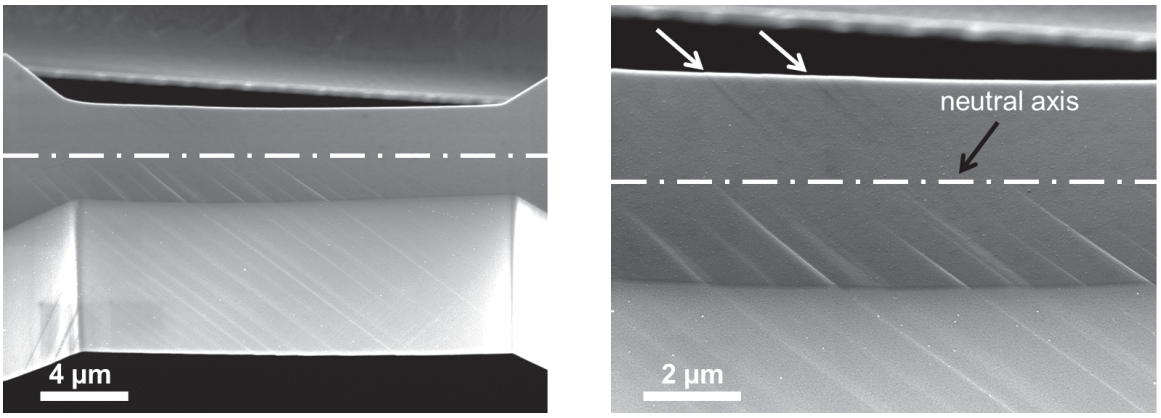


(a) (b)

**Figure 3.1** a) SEM image of the single crystalline bending beam A6 revealing distinct glide steps. The neutral axis is marked by a dashed white line. b) A detailed image of the region around the neutral axis. Slip steps in the compression side are marked by white arrows.

### 3.1.2 Type 2 - Bicrystalline

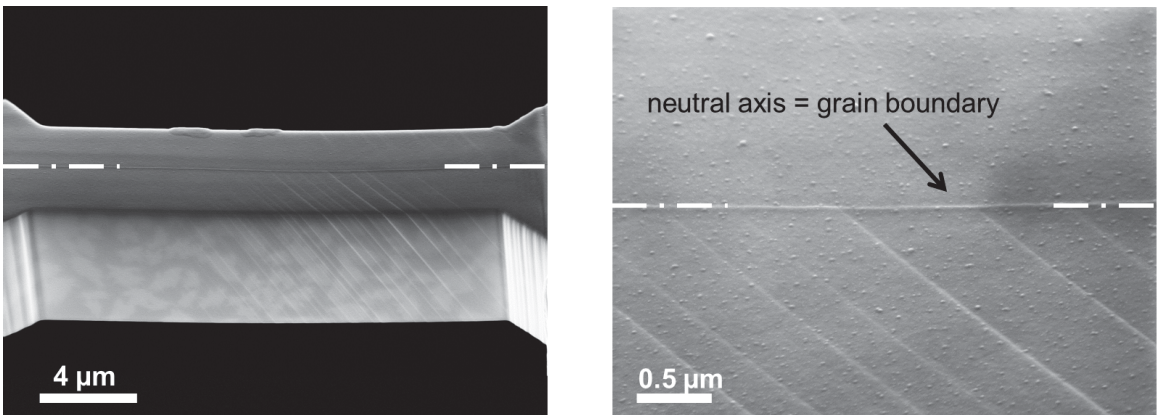


(a) (b)

**Figure 3.2** a) SEM images of the bicrystalline bending beam B1 revealing distinct glide steps. The neutral axis is marked by a dashed line, which is equal to the position of the grain boundary. b) A detailed image of the region around the neutral axis, where the slip steps stop at the neutral axis (grain boundary) in contrast to the single crystalline bending beam.

Glide steps can be observed at the tension and compression side of the bending beam, revealing a higher number at the fixed end of the bending beam (Fig. 3.2a, right side). Similar to the single crystalline sample they are more pronounced at the outer fiber, getting weaker towards the neutral axis. The glide steps stop at the neutral axis which is accompanied by a grain boundary (Fig. 3.2b).

### 3.1.3 Type 3 - Single crystalline with slit

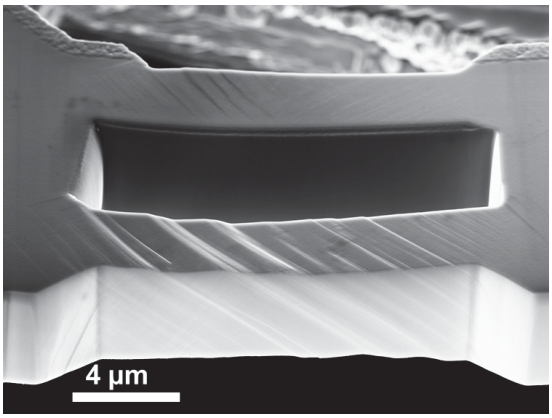


(a)

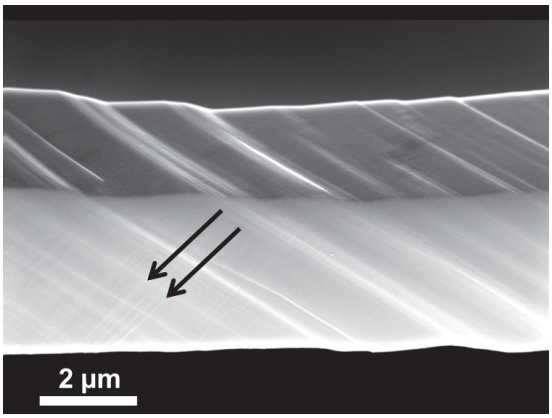


(b)

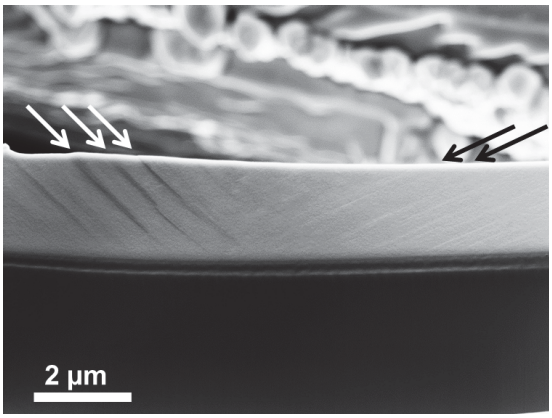


(c)

**Figure 3.3** a) SEM image of the single crystalline bending beam C4 with a slit along the neutral axis. Glide steps are uniformly distributed along the bending width. b) A detailed image of the tensile side of the bending beam, where distinct glide steps are formed. Weak glide steps from a second slip system are marked by black arrows. c) The glide steps in the compression side reveal different orientations on the left (marked by white arrows) and right side (marked by white arrows).

The slip steps are uniformly developed over the bending beam width and do not weaken towards the slit in the middle of the bending beam (Fig. 3.3a). On the tensile side of the bending beam (in the front) numerous, pronounced slip steps are observed. In the larger scaled image of the tension side further weak slip steps revealing a different orientation are obtained (Fig. 3.3b, black arrows). The slip steps in the compression side reveal different orientations on the left (white arrows) and the right side (black arrows) of the bending beam (Fig. 3.3c).

## 3.2 Stress-Strain Curves recorded at the Beamline

The stress-strain curves of the *in situ* $\mu$Laue experiments were measured with a user designed straining device as described in chapter 2.2.3. The data were analyzed by means of linear elastic bending beam theory (Chp. 2.4), evaluating the surface strain (Eq. 2.5) and the surface stress (Eq. 2.2) at the maximum value of the bending moment. For completeness the maximum surface stress of all samples is summarized in figure 6.3 in chapter 6.

### 3.2.1 Type 1 - Single Crystalline

Figure 3.4 presents the stress-strain curve of a single crystalline sample. The red dots indicate the readout of a full Laue pattern during the bending experiment. The first loading step with a plastic strain of $1.5*10^{-3}$ shows a distinct elastic plastic transition, similar to the second loading step with a plastic strain of $6.6*10^{-3}$ and the third loading step with a plastic strain of $1.3*10^{-2}$. The maximum surface stress of 150 MPa is reached in the third loading step at a strain of $9.3*10^{-3}$. A different slope is revealed for the elastic loading and the unloading curve.
The unloading curves consist of green dots marking the point of unloading, blue dots marking the point of zero load and black lines referring to ideal elastic unloading (linear fit of steepest part of the unloading curve).

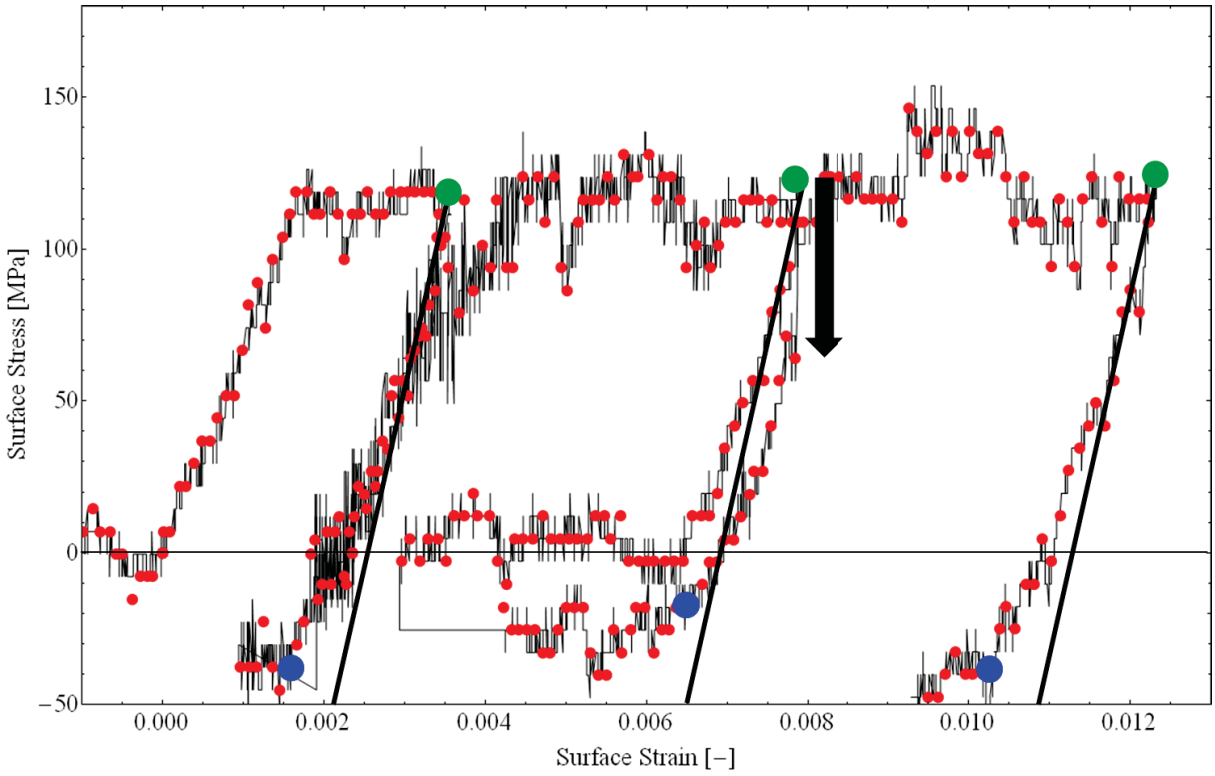


**Figure 3.4** Stress-strain curve of the single crystalline sample A5 with the points of unloading (green dots), points of zero load (blue dots) and the ideal elastic trend of the unloading curves (black lines). The black arrow in the second unloading curve marks a drop in the stress level.

The first and the third unloading curve show perfect elastic behavior down to a certain stress level, where they exhibit a smaller slope after a kink. At the point of zero load a reverse strain of $0.44*10^{-3}$ is achieved for the first loading-unloading step, which is a 22% reduction of the applied plastic strain. The deviation of the second unloading curve from the ideal elastic trend must not be attributed to an effect, as the whole unloading curve is shifted to a lower stress level (black arrow) due to a sudden thermal drift of the measured force.

### 3.2.2 Type 2 - Bicrystalline

The stress-strain curve of a bicrystalline sample loaded four times to a plastic strain of $1.7*10^{-2}$ is illustrated in figure 3.5. The maximum surface stress is approximately 270 MPa, reached at a strain of $7.3*10^{-3}$.

The unloading curves of the first loading step with a plastic strain of $1.5*10^{-3}$, as well as for the third loading step with a plastic strain of $1.33*10^{-2}$ and the fourth loading step with a plastic strain of $1.73*10^{-2}$ behave ideal elastic in the beginning of unloading. After the kink the unloading curves have a smaller slope, exhibiting a reverse strain at zero load. For the first deformation step a reverse strain of $0.16*10^{-3}$ is observed, which is an approximately 9% reduction of the applied plastic strain.

The third loading cycle is dropped to a lower stress level compared to the other deformation steps. It should be mentioned that beside of a softening during deformation, also unwanted side effects such as air conditioning affecting the tungsten wire of the load cell or gluing of the indenter with the bending beam could occur.

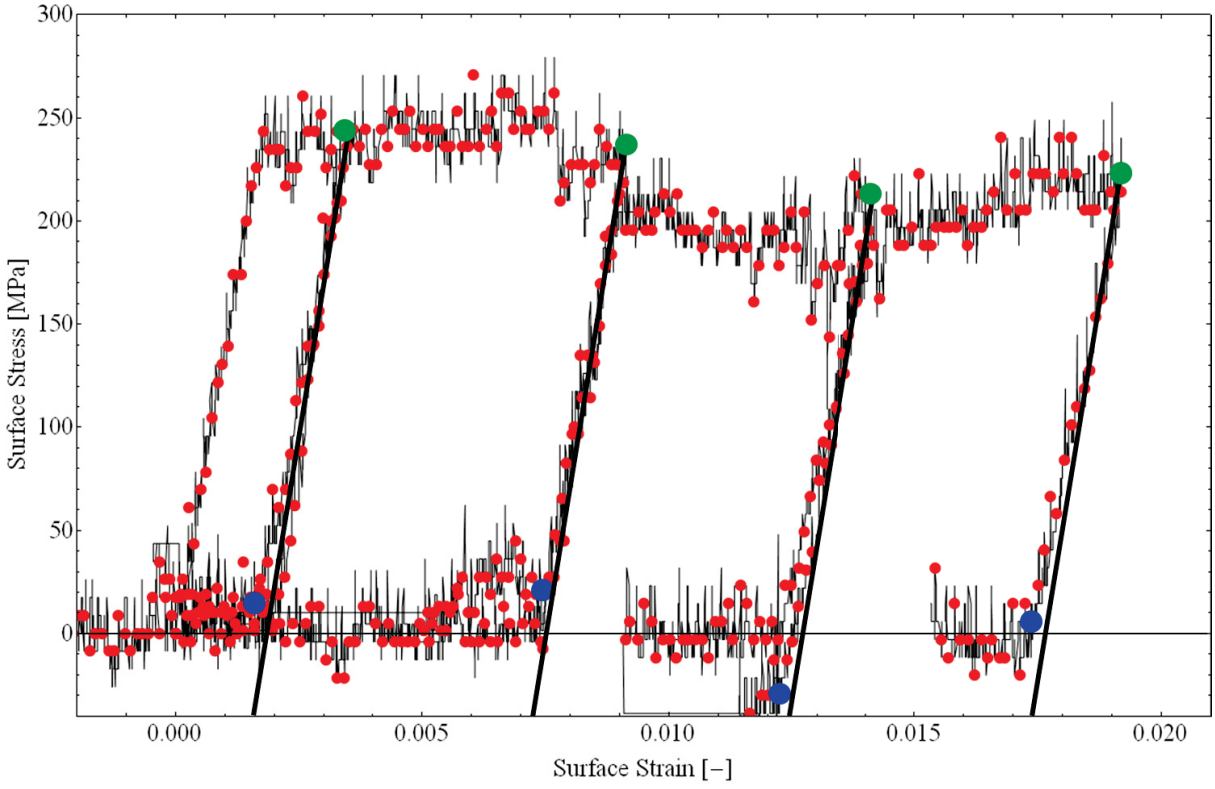


**Figure 3.5** Stress-strain curve of the bicrystalline sample B2. The plastic strain at zero load (blue dots) of deformation steps one, three, four shows a smaller value than predicted by the ideal elastic trend of the unloading curve.

### 3.2.3 Type 3 - Single Crystalline with Slit

The stress-strain curve of sample number C2 is shown in figure 3.6. Four loading and unloading steps with a plastic strain of $4.9*10^{-2}$ were performed. Hardening is missing throughout the four loading steps. The maximum load of 89 MPa is reached in the first loading cycle at a strain of $9.0*10^{-3}$. Compared with the single crystalline sample A5 and the bicrystalline sample B2 a noticeable decrease in the maximum stress.

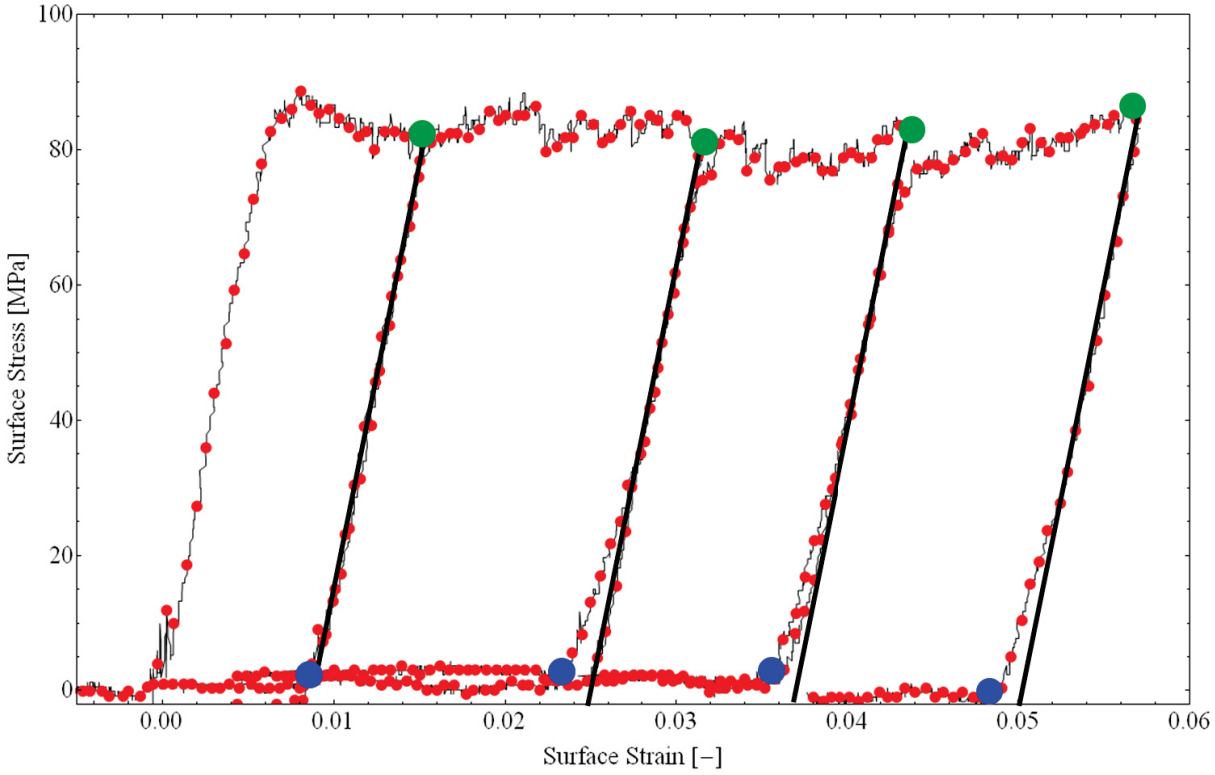


**Figure 3.6** Stress-strain curve of the single crystalline sample C2 with the slit, revealing a deviation of ideal elastic unloading for deformation steps two, three and four.

The unloading curve of the first loading step is almost fitting with the elastic prediction, with a reverse strain of $0.1*10^{-3}$, being a 1% reduction of the applied plastic strain. This is in contrast to the unloading curves of the second deformation step at a plastic strain of $2.3*10^{-2}$, the third step with a plastic strain of $3.6*10^{-2}$ as well as for the fourth step, showing a nonlinear unloading curve.

## 3.3 *In situ* Laue Observations

During the bending experiments $\mu$Laue patterns were continuously recorded, achieving the evolution of the peak position and the peak shape during loading and unloading. Thereby the beam was focused on one distinct position nearby the neutral axis of the single crystalline and bicrystalline bending beam in order to get information concerning the dislocation activity at the neutral axis. For the single crystalline bending beam with the slit a position on the tension or the compression side was investigated.
The particular interest lies in the change of the peak shape between the point of unloading and zero load. The evolution of the whole $\mu$Laue pattern will be represented by the evolution of one selected peak. For a significant investigation of the dislocation density evolution, especially during unloading, the elongation of the peak in $\xi$- and $\nu$-direction was quantified in terms of the $\mathrm{FWHM}_{\xi}$ (GNDs) and $\mathrm{FWHM}_{\nu}$ (SSDs).

### 3.3.1 Type 1 - Single Crystalline

The selected 044 peak is marked in the Laue pattern (Fig. 3.7a). The corresponding stress-strain curve is presented in figure 3.7b. At characteristic positions of the deformation process (marked by black numbers) the 044 Laue spots are presented in figure 3.8 with the red dots referring to the initial position of the peak:

- 1 Start of experiment
- 2, 5, 8 Elastic-plastic transition of deformation step 1, 2, 3
- 3, 6, 9 Point of unloading of deformation step 1, 2, 3
- 4, 7, 10 Point of zero load of deformation step 1, 2, 3

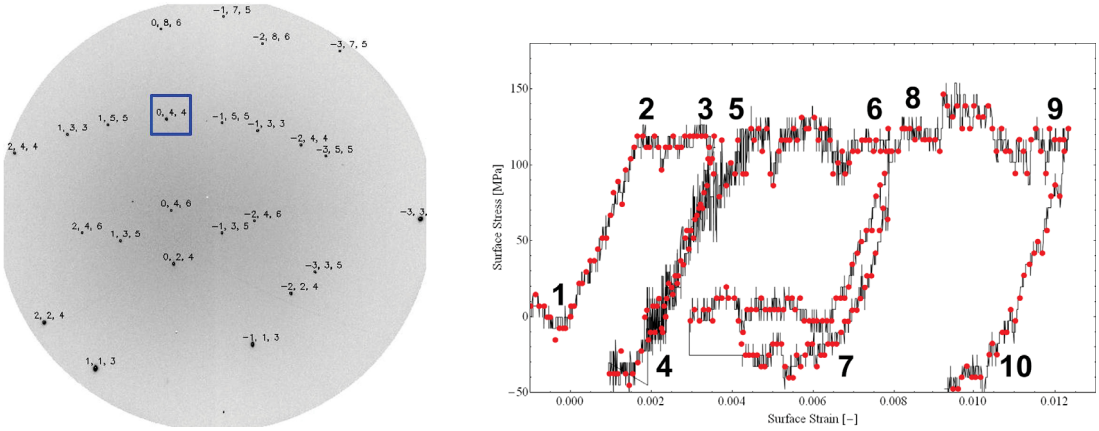


(a) (b)

**Figure 3.7** a) The indexed Laue pattern of sample number A5 in its undeformed state with the investigated 044 spot marked in blue. b) The stress-strain curve of sample number A5 with numbers indicating characteristic positions where the 044 spot is shown in figure 3.8.

The Laue peak in the undeformed state (number 1 in figure 3.8) has an elliptical shape and is not perfectly circular. During elastic loading (number 1 to 2, number 4 to 5, number 7 to 8) the peak reveals slight streaking in $\xi$-direction, leaving its initial position (shift of the peak). This trend continues during plastic loading (number 2 to 3, number 5 to 6, number 8 to 9) in which the amount of streaking in $\xi$-direction and the shift increases with rising number of deformation steps. Furthermore, a peak broadening in the $\nu$-direction can be observed. Regarding the first unloading step (number 3 to 4) the elongation of the peak is clearly reduced almost achieving a circular shape and the peak moves backwards approaching its original position.

It should be mentioned that the small tale on the right side of the peak separates during the second deformation process, keeping the same position with the same shape during the rest of the experiment. During the following unloading steps (number 6 to 7, 9 to 10) the elongation in $\xi$-direction is reduced, which is also true for a certain amount of the shift. However, the peak broadening in $\nu$-direction does not change a lot and the peak does not achieve its initial shape, nor its initial position after these unloading processes.

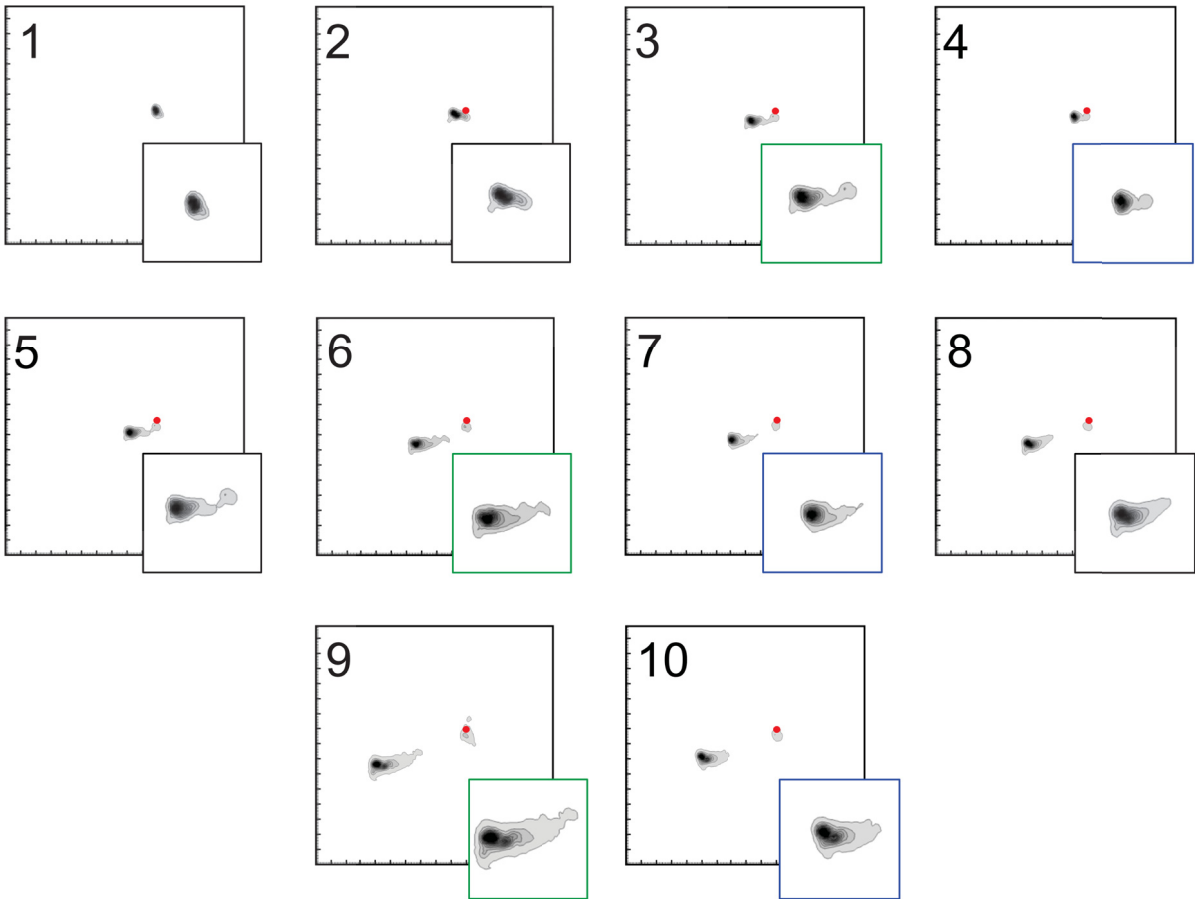


**Figure 3.8** The position and shape of the 044 Laue peak of sample A5 is shown in the undeformed state (1), at the elastic-plastic transitions (2, 5, 8), at the points of unloading (3, 6, 9) and the points of zero load (4, 7, 10). Peak streaking and shifting is observed during loading, which is removed during unloading to different amounts.

Figure 3.9 presents the $FWHM_{\xi}$ and the $FWHM_{\nu}$ versus total strain of the 044 peak during the first loading-unloading step. The $FWHM_{\xi}$ (blue dots) increases to a small amount during elastic loading. The same is true for the plastic regime even though to a greater degree. The unloading is characterized by a strong reduction of the $FWHM_{\xi}$ of approximately 93% almost reaching its initial value at $1.5*10^{-3}$ permanent plastic strain. The $FWHM_{\nu}$ (red rhombuses) slightly increases in the plastic loading regime, whereas it remains constant during unloading.

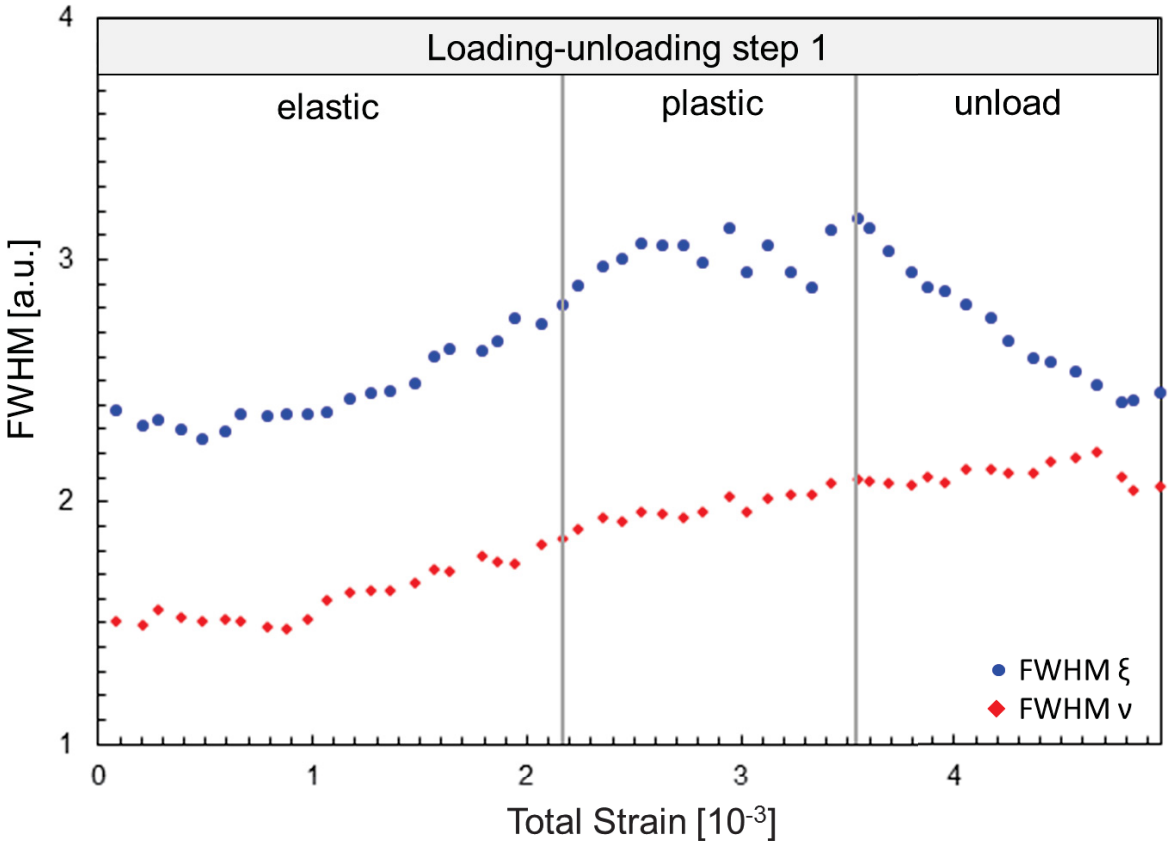


**Figure 3.9** The evolution of the $FWHM_{\xi}$ (blue dots) and the $FWHM_{\nu}$ (red rhombuses) versus total strain during elastic, plastic loading and unloading of the single crystalline sample A5 of the first deformation step with a permanent plastic strain of $1.5*10^{-3}$.

### 3.3.2 Type 2 - Bicrystalline

The evolution of the selected 224 peak shape during the four loading and unloading steps of a bicrystalline sample is investigated. The position of the 224 peak in the Laue pattern is enlightened in figure 3.10. The white colored indexation belongs to the first grain, the black colored indexation to the second grain. A stress-strain curve for sample B1 does not exist due to thermal drift caused by the airflow of the air conditioning system, which was further suppressed by shielding (see chapter 6.5).

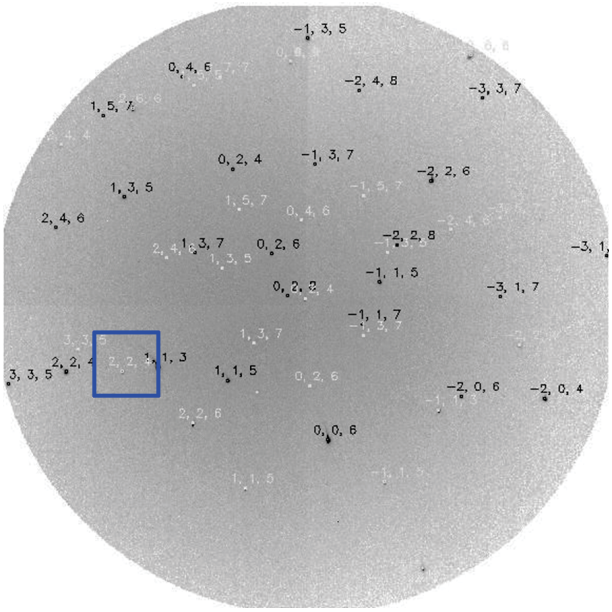


**Figure 3.10** The indexed Laue pattern of the bicrystalline sample B1 with the 224 peak (blue frame).

The red dots in figure 3.11 mark the initial peak position, whereas the numbers refer to certain positions in the deformation process, where the Laue patterns were recorded:

- 1 Start of experiment
- 2, 4, 6, 8 Points of unloading of deformation step 1, 2, 3, 4
- 3, 5, 7, 9 Points of zero load of deformation step 1, 2, 3, 4

During elastic and plastic loading (numbers 1 to 2 in figure 3.11) peak streaking in $\xi$-direction, a broadening in $\nu$-direction as well as a considerable shift of the peak takes place. At the point of zero load (number 3) the streaking in $\xi$-direction is strongly reduced unlike the broadening of the peak in $\nu$-direction. Also a back movement of the peak can be observed. During the following loading steps (numbers 3 to 4, 5 to 6, 7 to 8) further streaking and tremendous shifting of the peak is observed. Unloading of the sample (numbers 4 to 5, 6 to 6, 8 to 9) is characterized by a reduction in peak streaking and a clear back movement of the peak.

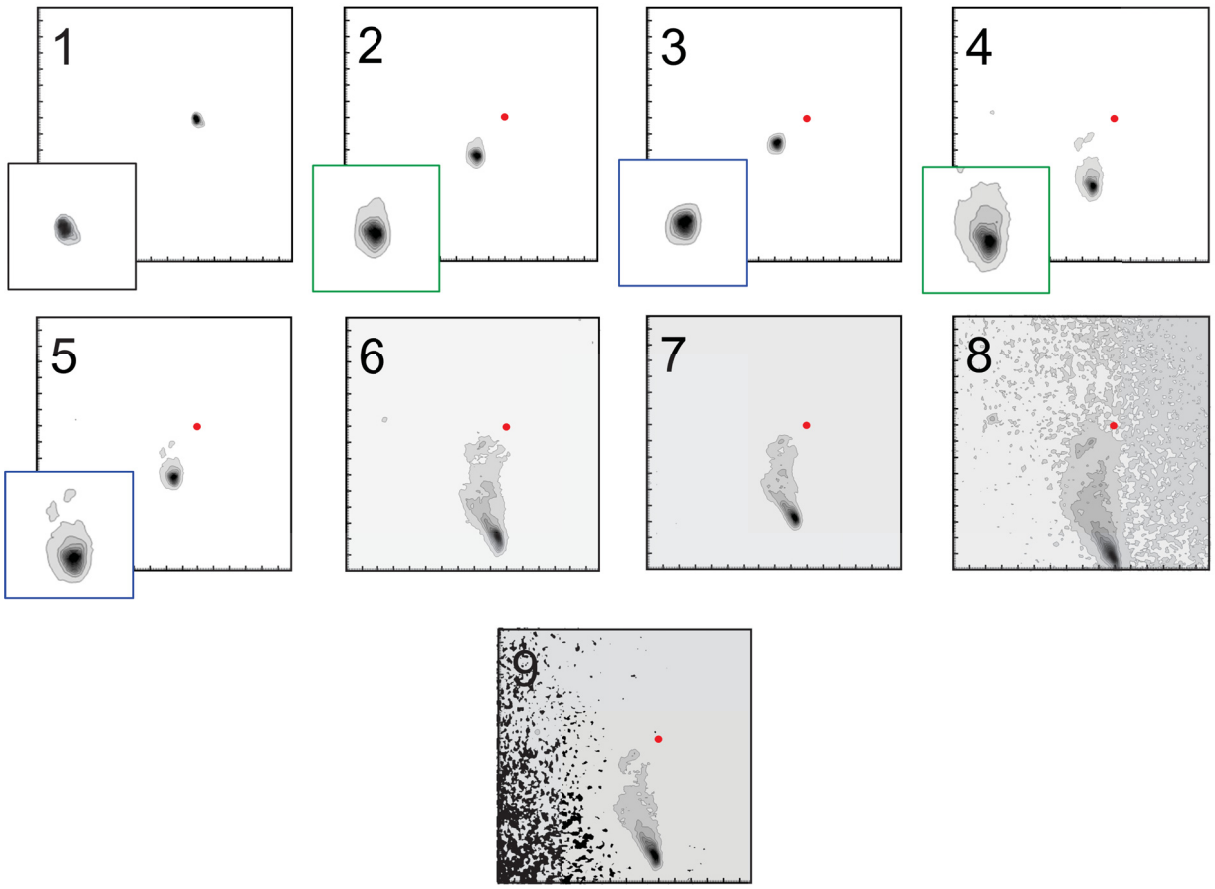


**Figure 3.11** The 224 peak of the bicrystalline sample B1 before deformation (1), at the point of unloading (2, 4, 6, 8) and at the point of zero load (3, 5, 7, 9). The grey and black background is due to a low intensity.

The $FWHM_{\xi}$ and the $FWHM_{\nu}$ versus total strain of the 044 peak during the first loading-unloading step is presented in figure 3.12. A slight increase of the $FWHM_{\xi}$ is achieved during the first elastic loading step, which is further increased in the plastic loading regime. From the point of unloading to the point of zero load the $FWHM_{\xi}$ is decreased to approximately 65% of its maximum value. The $FWHM_{\nu}$ increases during elastic and plastic loading and does not change significantly during unloading of the sample.

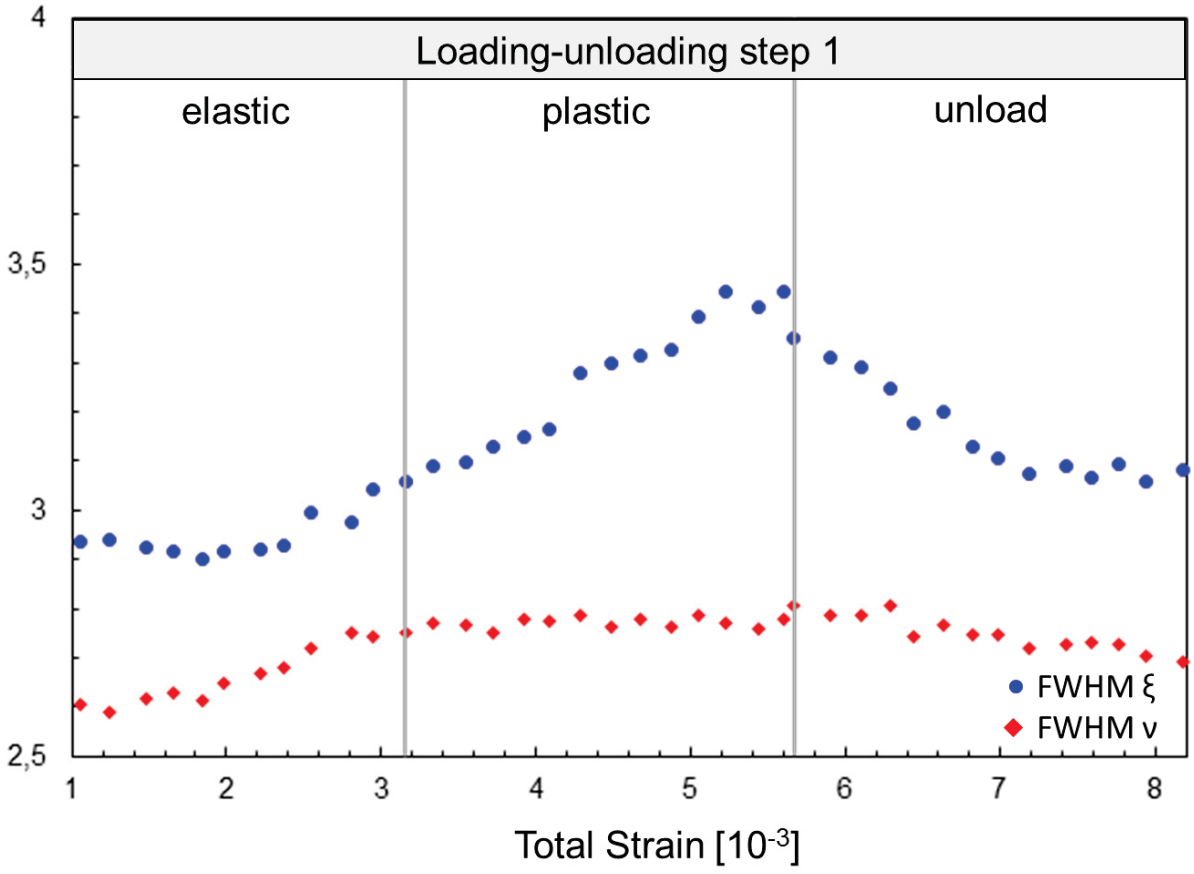


**Figure 3.12** The $FWHM_{\xi}$ (blue dots) and $FWHM_{\xi}$ (red dots) of the 266 peak is presented for the bicrystalline sample B1 during elastic, plastic loading and unloading of the first deformation step.

### 3.3.3 Type 3 - Single Crystalline with Slit

The evolution of the peak shape and position of the selected $\bar{1}15$ belonging to a single crystalline sample with a slit is presented. The indexed Laue pattern can be seen in figure 3.13a. The corresponding stress-strain curve is shown in figure 3.13b, with the black numbers marking the position, where the Laue spots were measured.

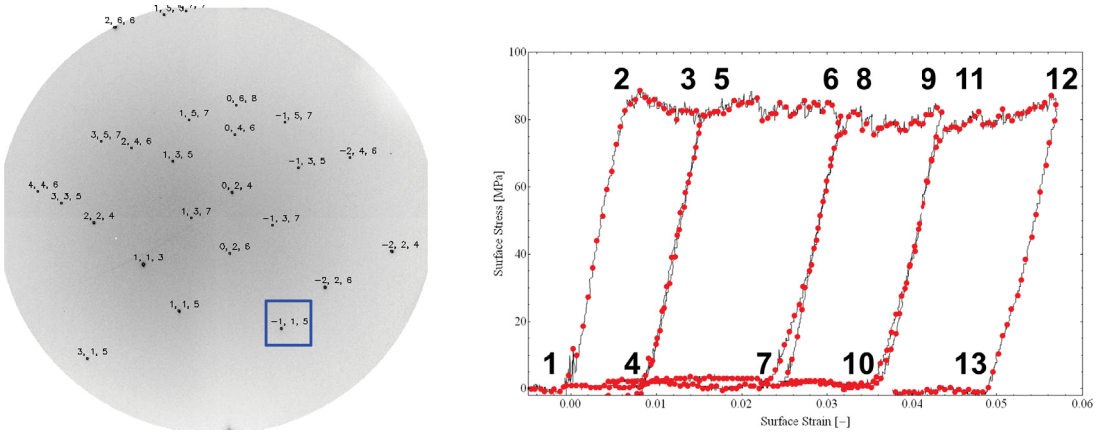


(a) (b)

**Figure 3.13** a) The indexed Laue pattern of sample number C2 before straining with the $\bar{1}15$ peak. b) The corresponding stress-strain curve of sample number C2 with black numbers indicating the positions of the presented Laue peaks in figure 3.14.

The initial peak shape (number 1 in figure 3.14) is almost perfectly circular. The first elastic loading step (number 1 to 2) results in a shift and streaking of the Laue peak in $\xi$-direction, which is increasing during plastic loading (number 2 to 3). The first unloading exhibits a distinct back movement and a minor reduction of the peak elongation (number 3 to 4). For further elastic (numbers 4 to 5, 7 to 8, 10 to 11) and plastic loading (numbers 5 to 6, 8 to 9, 11 to 12) a shift of the Laue peak is observed, whereas an elongation of the peak in $\xi$-direction is missing. The other unloading steps (numbers 6 to 7, 9 to 10, 12 to 13) reveal a slight back movement of the peak, whereas the peak shape does not change. Compared to the initial state the peak exhibits a distinct elongation in the $\xi$- and a slight one in the $\nu$-direction.

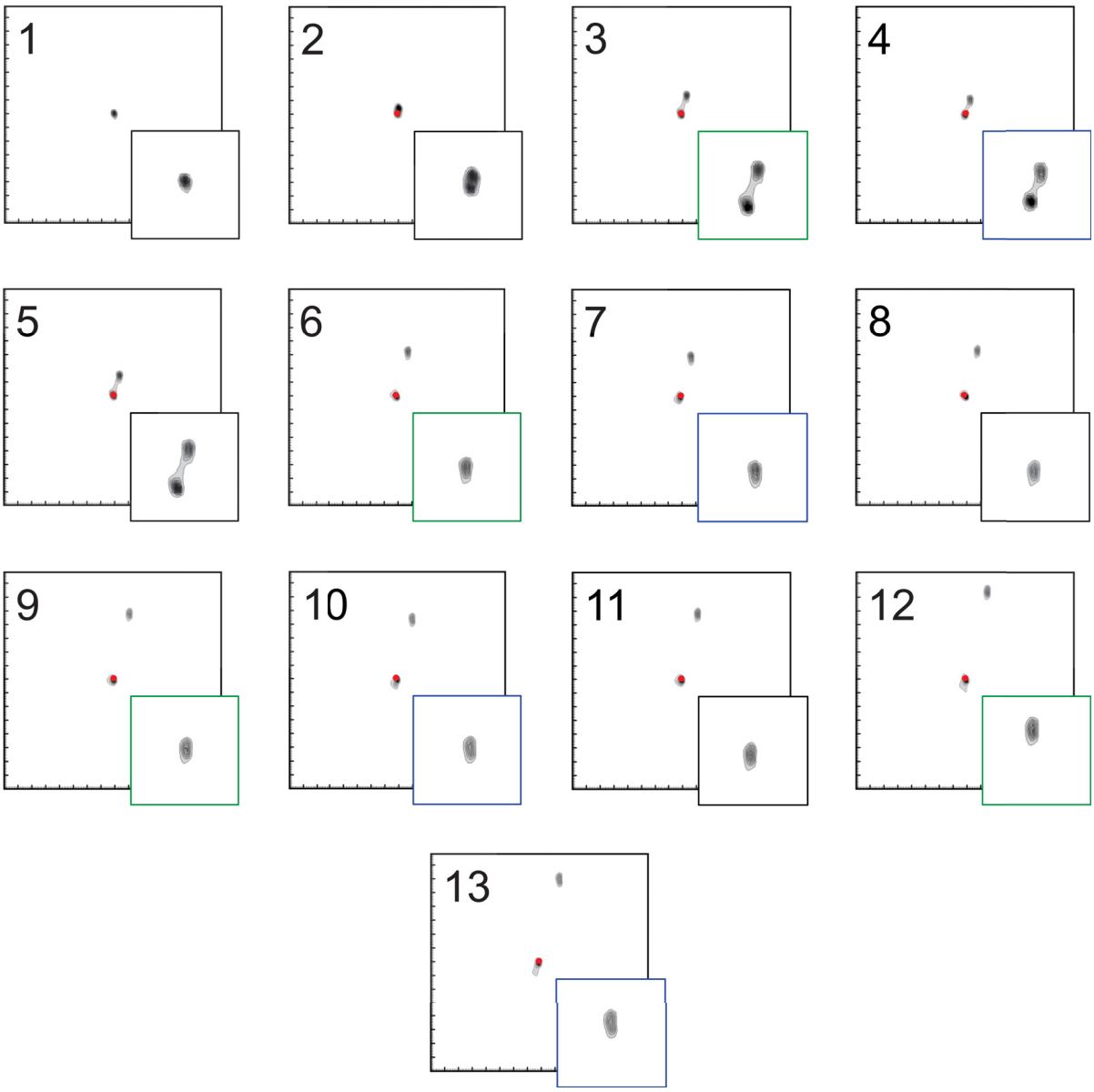


**Figure 3.14** Evolution of the $\bar{1}15$ Laue spot of sample C2: undeformed state (1), elastic-plastic transition (2, 5, 8, 11), unloading point (3, 6, 9, 12) and point of zero load (4, 7, 10, 13). Only little peak streaking in $\xi$-direction, but a distinct shift of the peak is present during elastic and plastic loading. Unlike the reduction of the peak streaking a back movement of the peak during unloading is observed for each unloading step.

For a quantitative interpretation of the streaking the $\mathrm{FWHM}_\xi$ and the $\mathrm{FWHM}_\nu$ versus total strain during the first loading-unloading step is given in figure 3.15. During elastic loading a fluctuating progression of the $\mathrm{FWHM}_\xi$ (blue dots) and $\mathrm{FWHM}_\nu$ (red rhombuses) is revealed,

moreless remaining on the initial value. The $FWHM_{\xi}$ clearly increases during plastic loading and stays constant, or at least slightly decreases during unloading.

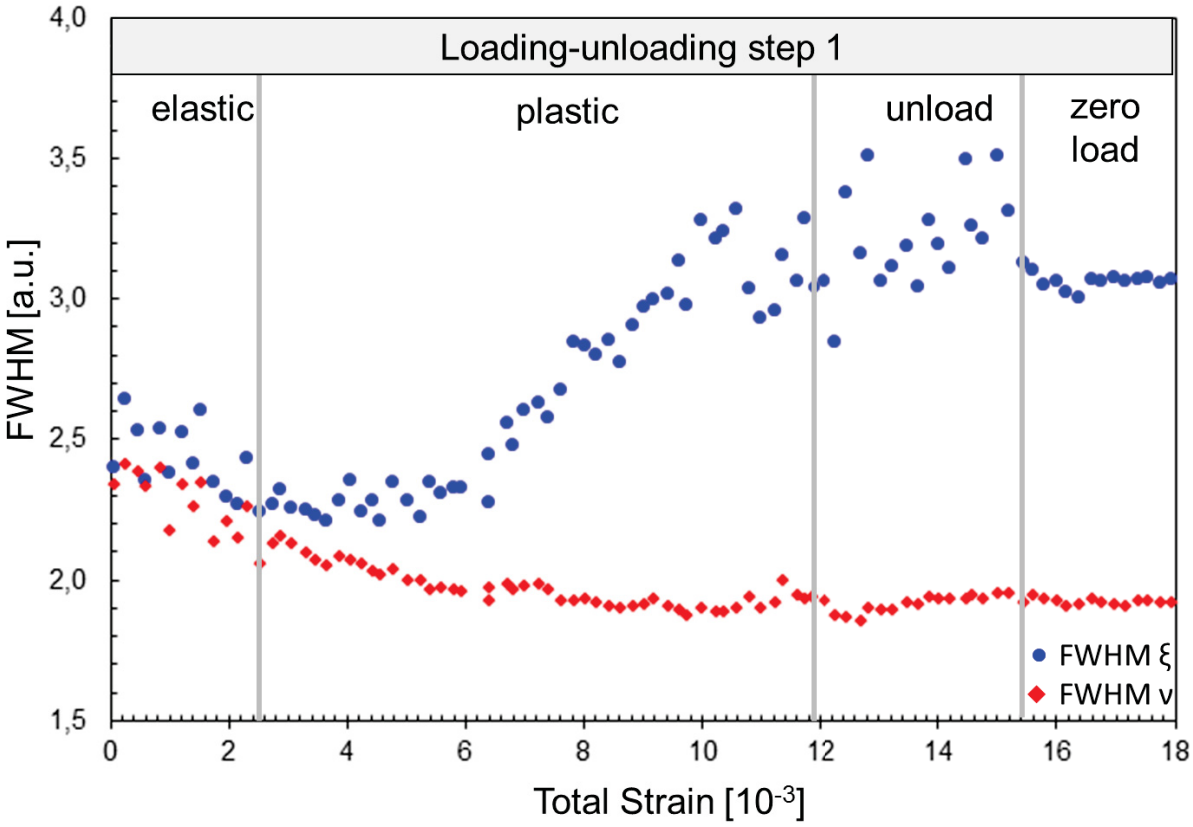


**Figure 3.15** Evolution of the $FWHM_{\xi}$ (blue dots) and $FWHM_{\nu}$ (red rhombuses) during elastic loading, plastic loading and unloading of the 224 peak of the single crystalline sample C1 with the slit.

## 3.4 Laue Mesh Scans

Similar to the in situ Laue measurements, a representative peak of the $\mu$Laue pattern was selected to show the peak shape evolution over the length and width of the bending beam.

### 3.4.1 Type 1 - Single Crystalline

The mesh scan of a single crystalline sample is presented in figure 3.16. The $\mu$Laue patterns were measured with a step size of 2 $\mu$m in the x-, y-direction at a plastic strain of $1.05*10^{-2}$ (number 10 figure 3.4b). The pink area with the higher intensity marks the area of the sample volume. On the left side the clamping is shown, the middle is characterized by the gauge section of the bending beam and the point of load incidence is on the right side.
The peak shape at the clamping and the right side of the bending beam gauge section is almost circular. Looking at the left end of the beam a distinct elongation of the upper peak is visible. The streaking decreases towards the non fixed end of the bending beam until the peak shape becomes circular again. Unlike the peaks along the neutral axis, the elongated peaks in the compression and tension side of the bending beam are curved.

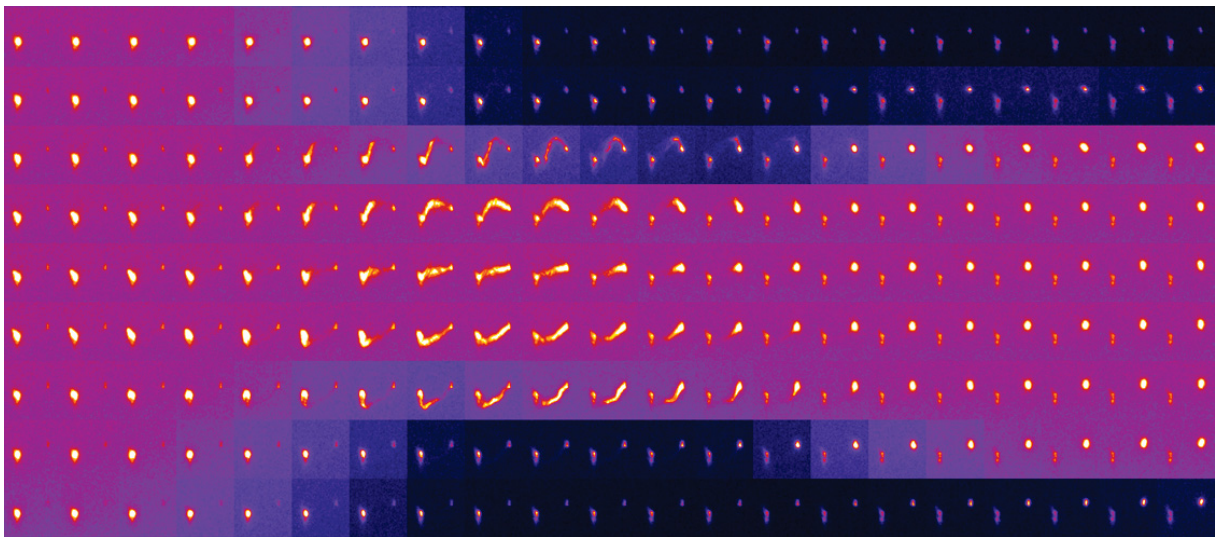

**Figure 3.16** Mesh scan of the single crystalline sample A5 with the selected 044 peak, exhibiting distinct streaking at the gauge section of the bending beam. The streaking is more pronounced at the clamped side.

### 3.4.2 Type 2 - Bicrystalline

The mesh scan of the bicrystalline sample B1 is presented in figure 3.17. The synchrotron beam was rastered over the sample with step sizes of 2 $\mu$m in x- and 1 $\mu$m in y-direction.

Again the pink area marks the sample volume with the bending beam gauge section in the middle, the clamping on the left side and the point of load incidence would be on the right side.
The mesh scan reveals the 024 peak, coming from the grain on the tension side (lower half) of the bending beam. The more intensive lower peak shows distinct streaking, which increases towards the fixed end of the bending beam and decreases towards the non fixed end of the bending beam, similar to the single crystalline sample. In the compression side (upper half) the peaks are almost circular.

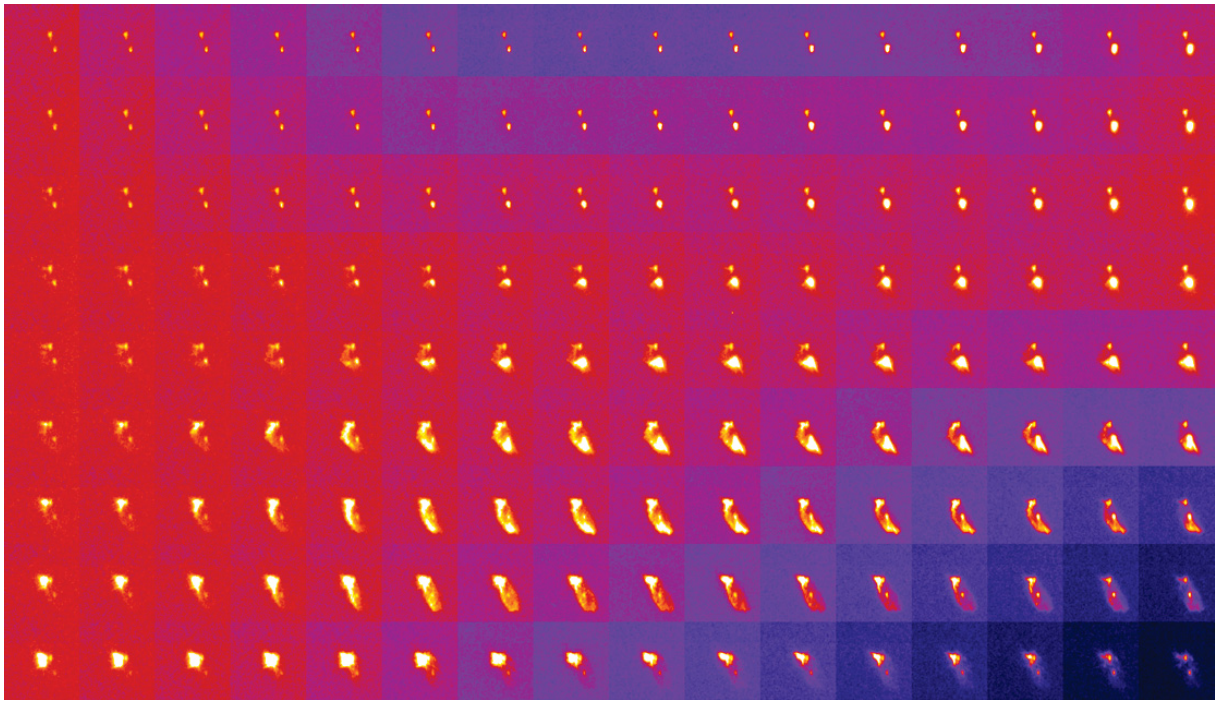

**Figure 3.17** Mesh scan of the bicrystalline sample B1 with the selected 024 peak belonging to the grain on the tension side.

### 3.4.3 Type 3 - Single Crystalline with Slit

The mesh scan of a single crystalline sample with a slit along the neutral axis is investigated at a plastic strain of $4.9*10^{-2}$. $\mu$Laue patterns were recorded every micrometer in the x- and y-direction. The clamping of the bending beam is on the left side and the point of load incidence on the right side of the picture. The bright area in the mesh scan (Fig. 3.18)

represents the sample area, where two single beams can be seen.
The compression side (upper single beam) reveals a distinct elongation of the lower peak, which is decreasing towards the non fixed end of the bending beam (right side). For the tensile side (lower single bending beam) an even more pronounced streaking is achieved accompanied by a certain curving, which is also strongly reduced towards the non fixed end, reaching a circular peak shape.

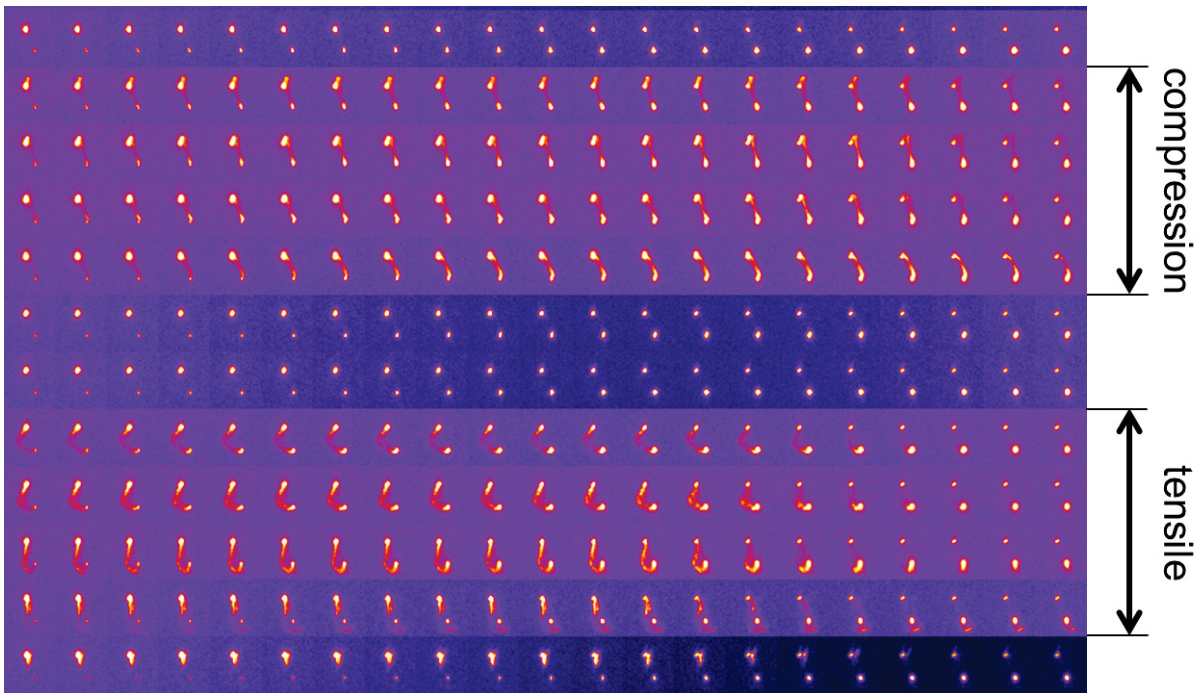


**Figure 3.18** Mesh scan of the single crystalline sample C2 with the slit along the neutral axis exhibiting distinct elongation of the peak. At the tension side the streaking is accompanied by a curving.

## 3.5 *In situ* SEM Stress-Strain Curves

Additional to the $\mu$Laue experiments *in situ* loading and unloading bending experiments were done with a Hysitron Pico Indenter PI 85 to achieve a better force resolution, which is described more precisely in chapter 2.3. The calculation of the stress-strain curves was done by means of linear elastic bending beam theory as described in chapter 2.4 with the surface strain (Eq. 2.5) and the surface stress (Eq. 2.2) evaluated at the maximum value of

the bending moment. Similar to the *in situ* $\mu$Laue bending experiments several loading and unloading steps were performed.

### 3.5.1 Type 1 - Single Crystalline

The single crystalline sample was tested in 35 loading and unloading steps up to a plastic strain of $2.97*10^{-2}$. In this chapter only the first 21 significant loading and unloading steps will be presented (Fig. 3.19).

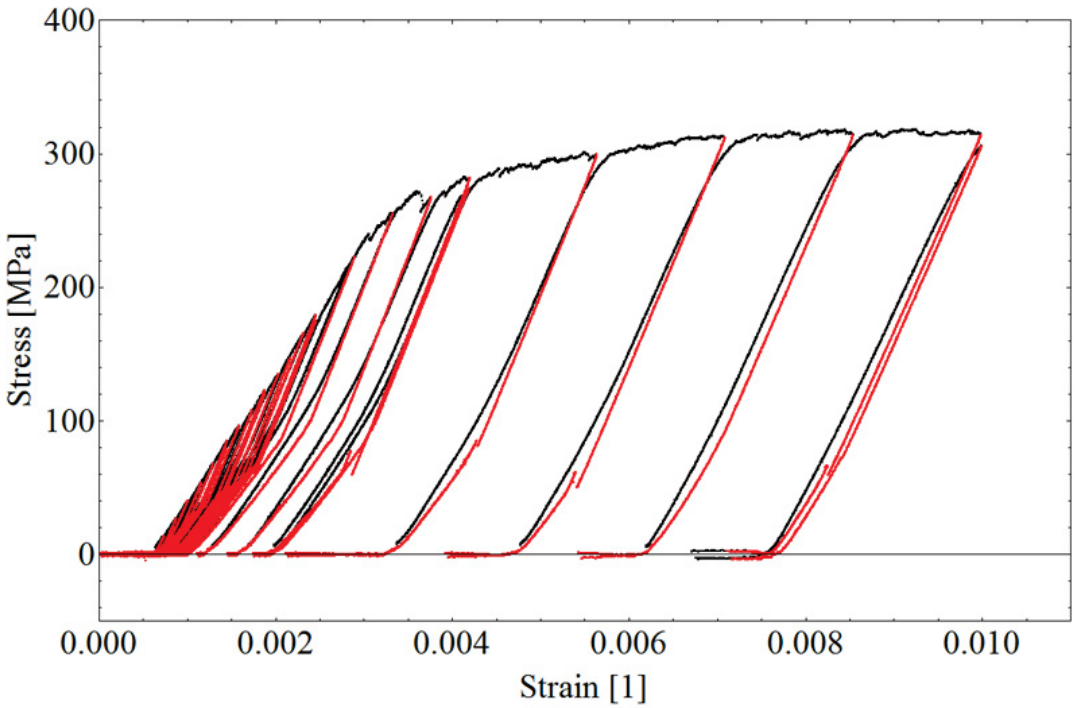


**Figure 3.19** Stress-strain curve of the single crystalline sample A6 tested with a Hysitron indenter. The black curves of the stress-strain curve measured with a Hysitron Pico Indenter represent the elastic and plastic loading, the red curves represent the unloading curves. Hardening and a kink in the unloading curve is observed shifting the unloading curves to lower strain levels than for ideal elastic behavior.

The black curves represent the elastic and plastic loading, the red ones the unloading response of the bending beam. The experiments were performed up to a plastic strain of approximately $7.6*10^{-3}$. Distinct hardening is observed up to a maximum stress of 320 MPa at a strain of approximately $1.0*10^{-2}$.
The elastic-plastic transition of the single loading curves is quite smooth. The unloading curves reveal an ideal elastic behavior in the beginning of unloading until the curve shows a kink. At the kink the unloading curve deviates from the ideal elastic trend revealing a reduction in plastic strain. This nonlinearity leads to a great difference in the strain of the measured unloading curves compared to their ideal elastic trend.
The stress level at which the kink occurs decreases with further loading, as well as the amount of reversible deformation.

### 3.5.2 Type 2 - Bicrystalline

The bicrystalline sample B4 was tested with 39 loading and unloading bending steps up to a plastic strain of $4.32*10^{-2}$. In this chapter only the first 22 deformation steps are presented (Fig. 3.20).
The sample shows distinct hardening with a maximum stress of approximately 345 MPa at a strain of $1.08*10^{-2}$. A kink in the elastic loading curve appears separating the loading curve in parts with a steeper and flatter slope. The first part of the elastic loading curve, with a flatter slope, exhibits a serrated progression due to dislocation activities, whereas the second part with the steeper slope is smooth. The elastic-plastic transition of the single deformation steps in the plastic loading regime is quite smooth. A serrated progression of the non ideal elastic part of the loading curve is revealed, similar to the single crystalline bending beam (Fig. 3.19). The unloading curves follow their ideal elastic trend within a confined stress regime. After a kink the unloading curves have a smaller slope than elastically expected and become serrated. The serrated flow in this regime is caused by a reversible back flow of GNDs. With ongoing deformation steps the amount of reversible back deformation decreases and the lower part of the unloading curve gets less serrated.

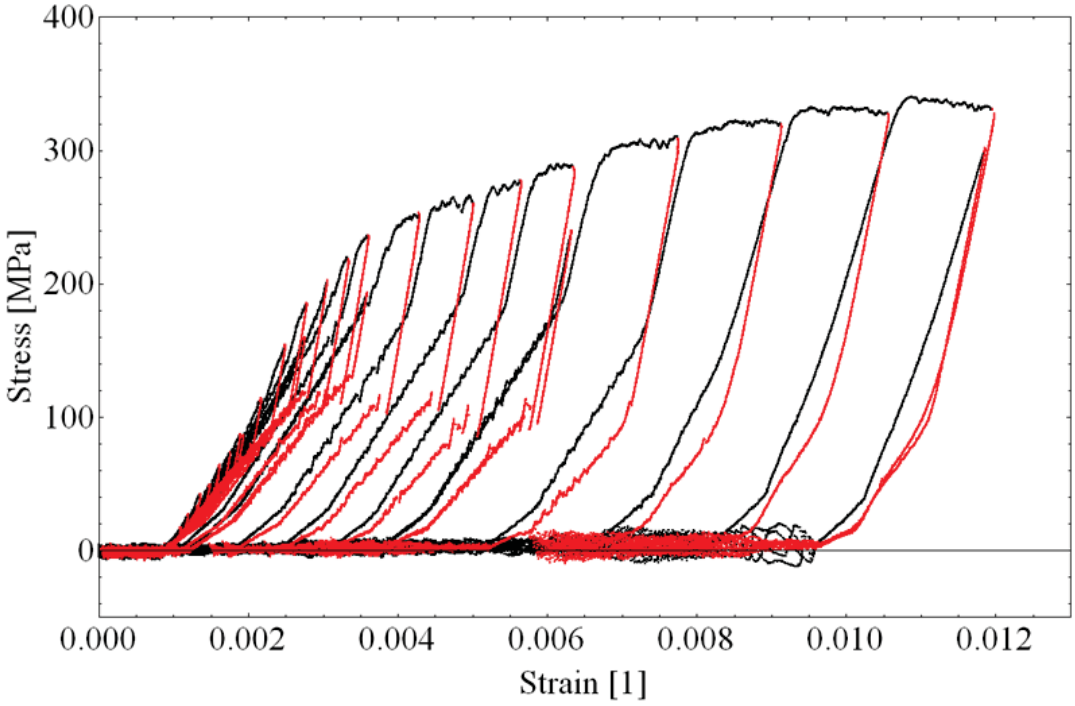


**Figure 3.20** Stress-strain curve of the bicrystalline sample B4. Kinks in the loading and unloading curves can be observed. The non ideal elastic part of the unloading curve is characterized by a jerky flow. The beginning of the elastic loading curve shows the same behavior. The reversible plastic strain weakens with ongoing deformation steps.

### 3.5.3 Type 3 - Single Crystalline with Slit

The single crystalline sample with the slit along the neutral axis was tested up to a plastic strain of $6.75*10^{-2}$. Altogether 45 loading and unloading steps were performed.
The sample was deformed up to a plastic strain of $1.93*10^{-2}$ in the first 24 deformation steps presented in figure 3.21. The stress-strain curve shows hardening up to a maximum stress of 280 MPa at a strain of $1.7*10^{-2}$. The stress level in the plastic regime drops between a strain of $6.0*10^{-3}$ and $8.6*10^{-3}$.

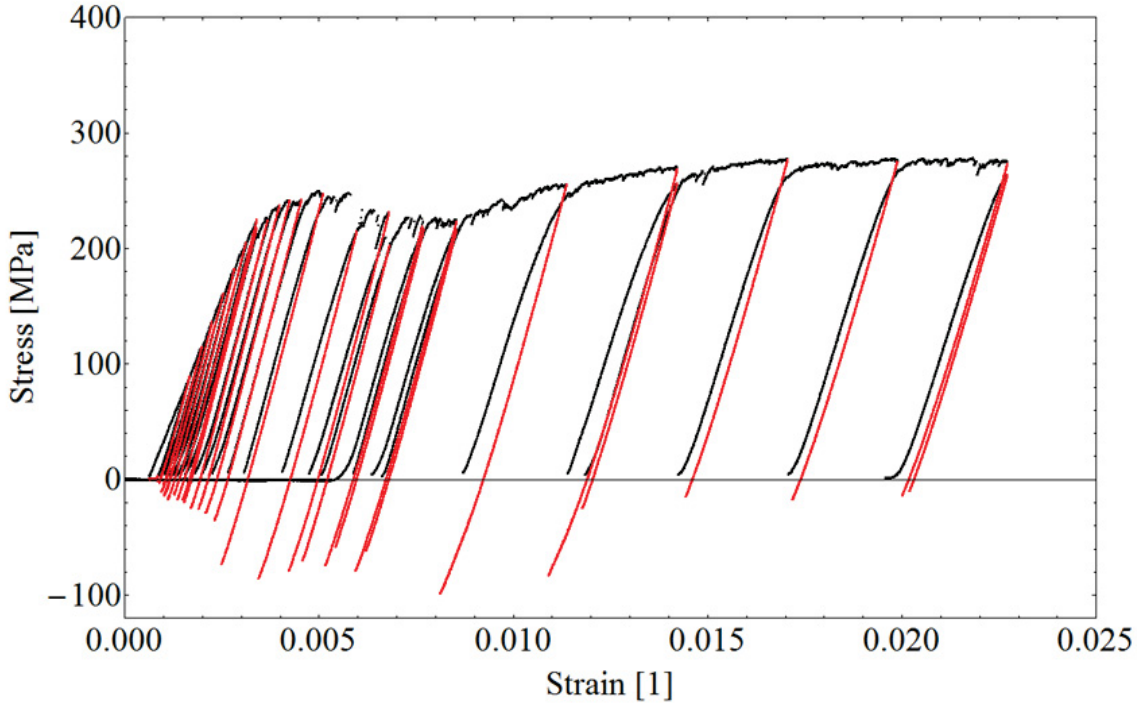


**Figure 3.21** Stress-strain curve of the single crystalline sample C4 with the slit along the neutral axis. The unloading curves show an ideal elastic behavior. See text for details.

Looking at the single deformation steps it can be seen that the slope of the loading curve remains steady. The elastic-plastic transition is quite distinct at a smaller deformation but getting smoother with ongoing deformation steps. In contrast to the other samples the red unloading curves do not show a kink, which is resulting in a plastic strain value that fits with its elastic trend. A jerky flow of the lower part of the unloading curves is absent as well. With the exception of the last five deformation cycles the unloading curves stop at large negative stress levels down to -100 MPa, which might be due to a gluing between the bending beam and the Berkovich indenter.

# Chapter 4

# Discussion

## 4.1 Type 1 - Single Crystalline

The nonlinear unloading curves observed in the $\mu$Laue bending measurements (Fig. 3.4) differ from those of micromechanical tensile or compression tests because of a different stress-strain gradient and, hence, a missing dislocation pile-up at a neutral axis. The reduction of elastic strain in the beginning of the unloading curve is similar to tension and compression tests. Though, after a kink elastic as well as plastic strain is reduced. This unloading behavior was already observed by [6, 8, 14] and fits well with the expectations given in chapter 1. The difference between the plastic strain applied during loading and the measured permanent plastic strain at zero load is called reverse strain. A reduction of the plastic strain by 22% is observed for the first deformation step revealing a significant amount of reverse plasticity during unloading.

According to bending experiments and additional 3D-DDD simulations from Motz et al. [6,9] the driving force for the reduction of plastic strain during unloading can be understood in terms of a backstress of piled up GNDs at the neutral axis. This backstress exhibits a different sign as the applied load and is superimposed to it. Thus, GNDs leave the sample as soon as the backstress exceeds the externally applied load, which is decreasing while unloading. Hence, the density of GNDs and the amount of plastic deformation must be reduced, if the GND movement is not hindered by obstacles like an oxide layer or by other dislocations.
The evolution of the FWHM$_\xi$ ($\propto \rho_{GND}$) during the first loading-unloading step (Fig. 3.9) supports the before mentioned results from Motz [6] and fits also with the nonlinear unloading

curve observed for the first deformation step. During plastic loading the FWHM$_\xi$ increases, indicating that GNDs are stored inside the bending beam in order to maintain the strain gradient. The correlation between the FWHM$_\xi$ and the density of GNDs $\rho_{GND}$ is given by equation 4.1 with the projection of the Burgers vector $b_p$, the diffraction vector $G_{hkl}$, the length of the primary beam path $L$ and the line element $u$ from [20, 27]:

$$FWHM_\xi = \rho_{GND} * b_p * \left|\underline{G_{hkl}}\right| * L * \sqrt{\left(1 - u * \frac{G_{hkl}}{\left|\underline{G_{hkl}}\right|}\right)^2} \tag{4.1}$$

From the point of unloading to the point of zero load the FWHM$_\xi$ and hence, the number of GNDs, is reduced to approximately 93% of its maximum value at a plastic strain of 1.5*10$^{-3}$, resulting in a reduction of plastic strain and a nonlinear unloading curve. For the second and third unloading step a similar behavior can be depicted from the qualitative interpretation of the peak streaking in the in situ Laue measurements (Fig. 3.8).
A $\rho_{GND}$ of 1.68*10$^{12}$ m$^{-2}$ is estimated to maintain a plastic strain of 1.5*10$^{-3}$ at zero load. The calculated $\rho_{GND}$ is interlinked to the surface strain $\epsilon_{surf} = \frac{x-l}{l}$, with $x$ being the length of the curved outer fiber after bending (assumption for the deformed region) and $l$ being the length of the original bending beam gauge section, by equation 4.2 from Motz [6]:

$$\rho_{GND} = \frac{1}{d_{GND}^2} = \frac{\omega}{x * b} \tag{4.2}$$

with the mean spacing between dislocations $d_{GND}^2$, the bending angle $\omega$ and the Burgers vector $b$. For simplification a simple dislocation structure as described in reference [6] is assumed.
A different quantity of reverse deformation is achieved, comparing the 22% reduction of plastic strain in the first unloading curve and the thereby measured 93% reduction of the FWHM$_\xi$. This difference is well possible since the stress-strain curve represents the deformation behavior of the entire bending beam gauge section and the diffraction data only a selected position on the bending beam [14].
The calculated FWHM$_\xi$ in this experiment is low, which can be attributed to (i) the central position of the selected peak in the Laue pattern, revealing weaker streaking because of the less enlargement of the projected streaking or (ii) minor dislocation activities in the probed region, which is possible far from the clamping of the bending beam (decreasing bending moment). Considering that for the in situ Laue measurements the middle of the bending beam gauge section was probed, this may have a fewer influence as the unfavorable selected peak.

The main disadvantage of the low $FWHM_{\xi}$ value is its scattered progression, hindering a clear quantitative interpretation.
The $FWHM_{\nu}$ increases during loading, showing that the total dislocation density (GNDs and SSDs) is increased. During unloading the total dislocation density is approximately constant, which can be explained by the missing long-range stresses (pile-up stress, backstress) of SSDs as described by Kirchlechner et al. [14]. It is also mentioned that the $FWHM_{\nu}$ has to be interpreted carefully, as $\mu$Laue is mainly sensitive to GNDs and not to SSDs.

Increased streaking occurs towards the clamping of the bending beam according to the mesh scan (Fig. 3.16). Furthermore, enhanced GND storage can be found in this region due to the maximum of the bending moment. Nearby the neutral axis (lower stress) the streaked peaks exhibit a single streaking axis, whereas at the outer fiber (higher stress) the peak streaking is characterised by a certain curving. According to Kirchlechner et al. [17] this is an indicator for the contribution of another slip system, which is also observed in the SEM image of the deformed bending beam (Fig. 6.1). The origin of the second glide system will be discussed at a later stage.
For completeness the appearance of the two peaks with different intensities in each box of a mesh scan should be explained. Because of the tale of the synchrotron beam [16], crystal planes from the bending beam gauge section (lower peak) and the bulk volume (upper peak) contribute to the Laue pattern, resulting in two peaks per box. The intensities are changing depending on their position along the bending beam. Thus, the peak from the bending beam gauge section (lower peak) reveals a higher intensity at the volume of the bending beam gauge section and a lower one at the volume of the sample base. A contrary behavior is achieved for the peak resulting from the bulk volume (upper peak).

Distinct glide steps observed in the SEM image (Fig. 3.1a) confirm major dislocation activity and therefore stronger peak streaking towards the clamping of the beam from the mesh scan. An important point is, that the glide steps do not pass through the whole bending beam, which agrees with the 3D-DDD simulations from Motz et al. [6, 9]. The glide steps do not abruptly stop in the middle of the bending beam, which indicates that the neutral axis is not an impenetrable barrier for dislocations.
The appearance of a second activated slip system in the SEM image, as well as in the mesh scan is consistent with the inverse pole figure (Fig. 2.3). The orientation of the sample A5 (red dot) is nearby the connecting line between the corner orientations (001) and (011), where

the Schmid factor for the primary and the secondary slip system are of equal magnitude.
Usually it is expected that the reversibility of the dislocation pile-up is weakened if more than one slip system is activated for the following reasons: (i) GNDs are more homogenously distributed during multiple slip, leading to a lower pile-up stress and a weaker backstress on the GNDs. As the driving force for reverse flow is thereby reduced, a smaller reduction of the FWHM$_\xi$ and of plastic strain would be assumed. (ii) The dislocation interaction between the primary and the secondary slip system hinders GNDs to leave the bending beam during unloading, leading to a weakened reversibility of GNDs. However, the pronounced reversibility observed in the stress strain curve and in the diffraction data claims that multiple slip may not play a predominant role at low strain values, in case that there is no interaction between the two glide systems.

The stress-strain curves observed by *in situ* SEM measurements with a high force resolution (Fig. 3.19) prove the nonlinear unloading curves and the appearance of reverse strain observed in the $\mu$Laue experiments. The amount of reverse strain is reduced with increasing number of deformation steps, which can be explained by an increase of the total dislocation density, also observed for the FWHM$_\nu$ ($\propto \rho_{total}$) during loading (Fig. 3.9). It is reasonable that thereby the possibility for dislocation interactions increases as well, hindering the GNDs in the pile-up to leave the sample during unloading.

## 4.2 Type 2 - Bicrystalline

The unloading curves of the $\mu$Laue measurements from sample B2 also show a nonlinear behavior, similar to the single crystalline sample (Fig. 3.5). It was expected that the grain boundary acts as an impenetrable barrier, causing a higher pile-up stress and hence an amplified reversibility of the dislocation pile-up. The SEM image (Fig. 3.2) proves, that the GNDs cannot overcome the neutral axis (grain boundary). Nevertheless, the 9% reduction of applied plastic strain at zero load of the first deformation step is weaker compared to the one of the single crystalline sample (22% reduction of plastic strain).
It should be mentioned, that the presented single crystalline sample A5 and the bicrystalline sample B2 were FIB milled out of different macrosamples. The orientation of the sample B2 is given in the inverse pole figure (Fig. 4.1a).
The first grain of sample B2 is close to a multiple slip orientation, as it is nearby the connecting

line of the corner orientations (001) and (011), indicating a minor difference between the Schmid factor of the primary and secondary slip system. For the second grain the difference between the Schmid factor of the primary and secondary slip system is larger, indicating that dislocations will only be generated on the primary slip system until a certain resolved shear stress is realized on the secondary slip system.

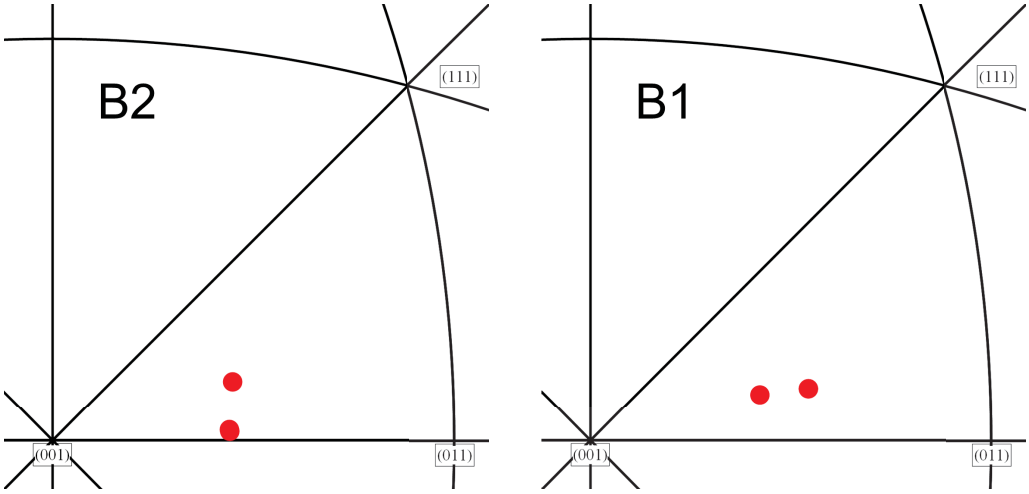


(a) (b)

**Figure 4.1** a) The orientation of the two grains in the bicrystalline sample B2 and b) in sample B1 marked by red dots in the inverse pole figure. The difference in orientation B1 and B2 is currently unresolved.

The orientations of the two grains in sample B2 influence and possibly weaken the reversibility of the dislocation pile-up. The localized GND distribution in the single slip oriented grain gains a higher pile-up stress and in fact an amplified reverse motion of GNDs. The more homogenous GND distribution in the multiple slip oriented grain leads to a smaller pile-up stress and a weakened reverse motion of GNDs. During unloading the multiple slip oriented grain will mainly show elastic back deformation, leading to the formation of global residual stresses.

The diffraction data of sample B1 show an increase of the $FWHM_{\xi}$ during the first loading step (Fig. 3.12), revealing that GNDs are stored. After unloading the $FWHM_{\xi}$ is reduced to approximately 65% at zero load. Similar to the unloading behavior of the stress-strain curves, the expected amplification of the effect did not occur, compared to the single crystalline sample

(93% reduction of $FWHM_\xi$ at $1.5*10^{-3}$ strain).

There are several influencing factors potentially causing the missing amplification: (i) Bending beam was probably probed at a position with a smaller backstress, leading to a smaller reduction of the $FWHM_\xi$. (ii) The higher stress level achieved for sample B1 can cause cross slip of the GNDs. Consequently the pile-up stress would be reduced, leading to a weaker reverse flow of GNDs during unloading. (iii) A second activated slip system, which is not unlikely at higher strain levels considering the orientation of sample B1 (Fig. 4.1b), would lead to a lower pile-up stress and consequently also reduce the back flow of GNDs during unloading. (iv) A higher strain of $5.7*10^{-3}$ at the point of unloading compared to $3.5*10^{-3}$ of the single crystalline sample A5, leads to a higher total dislocation density as seen by the increased $FWHM_\nu$, supporting dislocation interactions and hindering GNDs to leave the sample during unloading. (v) In general the type of grain boundary plays an important role too, as it is possible that dislocations are absorbed by the grain boundary and cannot contribute to the pile-up stress anymore, leading to a weakening of the effect. (vi) Due to elastic anisotropy the elastic constants are different in the first and the second grain. Thus, one grain would in principal deform in a greater amount, with the other deforming purely elastic. Thus, during unloading global residual stresses form. Furthermore, the neutral plane is not in the sample center as assumed.

As a stress-strain curve for the bicrystalline sample B1 is missing, an explicit comparison with mechanical data is not feasible. The comparability between the bicrystalline samples B1 and B2 is restricted by their different orientations (Fig. 4.1). Nevertheless, both samples are showing a smaller reversibility of dislocation pile-ups compared to the single crystalline sample A5 in terms of a smaller reduction of plastic strain from sample B2 and of the $FWHM_\xi$ from sample B1.

The evolution of the $FWHM_\nu$ reveals a distinct increase of the total dislocation density during plastic loading. The higher dislocation density supports dislocation interactions, which has a major influence on the back flow of GNDs during unloading (see (iv) in former paragraph). During unloading the $FWHM_\nu$ is not noteworthy decreased, revealing that SSDs, lacking long-range stresses, do not leave the sample during unloading.

For the *in situ* SEM measurements the single crystalline, bicrystalline and the single crystalline sample with the slit were manufactured out of the same macrosample exhibiting similar orientations, which improves the comparability of the different sample types. The unloading curves of the *in situ* SEM measurements of the bicrystalline sample (Fig. 3.20) reveal not only an increased amount of reverse strain, but also the onset of plastic back deformation at

higher stress levels, which fits to the expectations given in chapter 1. This can be explained by an increased pile-up stress, which would also be an evidence for the higher stress level of this stress-strain curve compared to the single crystalline sample. Furthermore a serrated flow is revealed after the kink in the unloading curve similar to the plastic regime, which can be attributed to an avalanche-like back flow of GNDs [14]. With increasing deformation the amount of reverse strain, as well as the serrated characteristic of the unloading curve is decreased, indicating that less GNDs leave the bending beam during unloading. This can be well possible, as the accumulating number of generated dislocations supports dislocation interactions, making it more difficult for GNDs to leave the bending beam during unloading. This is supported by the $\mu$Laue data, revealing an increase of the total dislocation density, which is not considerably reduced during unloading.
The observed amplification of the effect, shows that the grain boundary leads to a greater pile-up stress and hence to a greater backstress on the GNDs. This makes clear that the before mentioned absorption of dislocations (point (v) of previous paragraph) of the grain boundary cannot play a predominant role in these samples.

## 4.3 Type 3 - Single crystalline with slit

The $\mu$Laue measurements reveal an almost ideal elastic behavior of the unloading curve for the first loading-unloading step (Fig. 3.6), with an approximately 1% reduction of applied plastic strain at $9.0*10^{-3}$ plastic strain. For the other deformation steps an unexpected nonlinear unloading curve is achieved (Fig. 3.6), which is not seen in the *in situ* SEM experiment (Fig. 3.21). However, first we concentrate the discussion on the diffraction profile of the *in situ* Laue data.
Unfortunately, the peaks of the corresponding in situ Laue measurements from sample C2 are not exclusively showing the dislocation activity from the bending beam gauge section, but also from the sample base and sample head. This is indicated by a missing peak streaking of the selected peak in the in situ Laue measurements (Fig. 3.14) observed for deformation steps two to four, although the rotation of the peak reveals that the probed region was deformed.
Thereby the enlarged rectangular beam shape due to thermal drifting is of great importance, as it differs from the approximately 1x1 $\mu m^2$ beam size from the beginning (Fig. 4.2a). The beam dimensions calculated on the base of fluorescence data, is in the range of 1 $\mu$m in the y-direction and extended to a size of 9.4 $\mu$m at the FWHM in the x-direction (Fig. 4.2b). According to Kirchlechner et al. [16] the tale of the beam covers a more widespread area,

which causes not only crystal planes of the gauge section to contribute to the Laue pattern, but also the sample head and base leading to the appearance of three peaks. The bending beam gauge section typically contributes to the Laue pattern with a smaller volume and hence intensity compared to the sample base and head. Thus, the peak from the bending beam gauge section, describing the dislocation activity during the deformation process, can be overlooked, leading to a misinterpretation of the diffraction data.

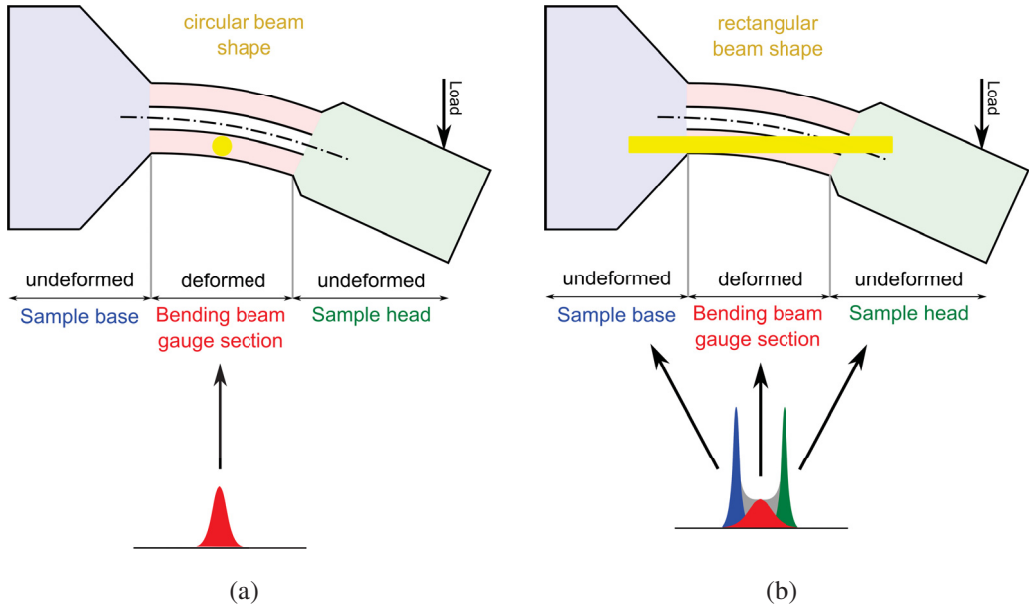


(a) (b)

**Figure 4.2** a) Schematic drawing of the ideal circular synchrotron beam shape (yellow) revealing one peak coming from the bending beam reduction (red) in case of sufficient large sized samples. b) Rectangular synchrotron beam shape (yellow) causes one peak from the sample base (blue), one peak from bending beam gauge section (red), one peak from sample head (green). Unlike the peak from the bending beam gauge section, the peaks from the sample head and base are not streaked. The peak from the bending beam gauge section reveals a lower intensity due to a streaking (intensity is scattered) and because it contributes to the Laue pattern with a smaller volume than sample head and base.

Consequently, for the quantification of the peak streaking in terms of the $FWHM_{\xi}$ and the $FWHM_{\nu}$ another sample C1 had to be used, which is not showing the before mentioned problems (see Appendix, fig. 6.2). The fluctuation of the $FWHM_{\xi}$ (Fig. 3.15) during the first unloading step hinders a clear quantification during the unloading process. Nevertheless an almost constant, probably slightly decreasing, progression of the $FWHM_{\xi}$ is revealed. This is in good agreement with the unloading behavior observed for sample C2 (Fig. 3.6)

showing an approximately 1% reduction of plastic strain. The weaker reverse flow of GNDs during unloading can be attributed to a lower pile-up stress, which is caused by the continous escape of dislocations at the inner sample surface during loading. This is confirmed by the missing increase of the $FWHM_{\nu}$ during loading, proving that the total dislocation density is not considerably increased.

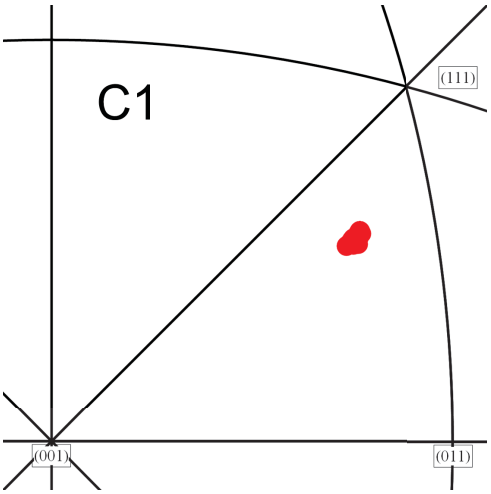


(a)

**Figure 4.3** Inverse pole figure of the single crystalline sample C1 with a slit along the neutral axis reveals a single slip orientation. The scattered data is due to a misorientation gradient inside the undeformed sample, probably due to unintended prestraining.

The slight decrease of the $FWHM_{\xi}$ during unloading can be attributed to a low pile-up stress of GNDs, which did not leave the sample during loading. The increase of the $FWHM_{\xi}$ during plastic loading indicates that a certain amount of GNDs is stored for the following reasons: (i) GNDs realizing a strain gradient, (ii) free glide of GNDs can be hindered on glide planes which are restricted by the sample head and base, similar to compression tests of Kirchlechner et al. [16]. The less pile-up stress observed for this sample type gives also an explanation for the reduced stress level compared to the single crystalline one in the $\mu$Laue and the *in situ* SEM stress-strain curves. Again the *in situ* SEM measurements reveal the expected ideal elastic unloading curves showing insignificant reverse strain at zero load, which is also proving the results from the $\mu$Laue measurements during the first deformation step. The drop of the stress level at a strain of $6.0*10^{-3}$ reveals a softening, due to dislocations escaping to the bending beam surface.

## 4.4 Comparison with Expectations

To summarize, the mechanical data of the $\mu$Laue experiments concerning the amplification (bicrystalline) and the weakening (single crystalline with slit) of the reversibility of dislocation pile-ups are not perfectly fitting with the expected behavior presented in chapter 1. For the bicrystalline sample the diffraction data do not reveal the expected amplification of the reversibility, whereas the expected weakening is observed for the single crystalline sample with the slit.

The unloading curves of the *in situ* SEM experiments, exhibiting similar orientations prove the expected behavior, which can be seen by comparing figure 4.4 with the schematic drawing given in figure 1.4.

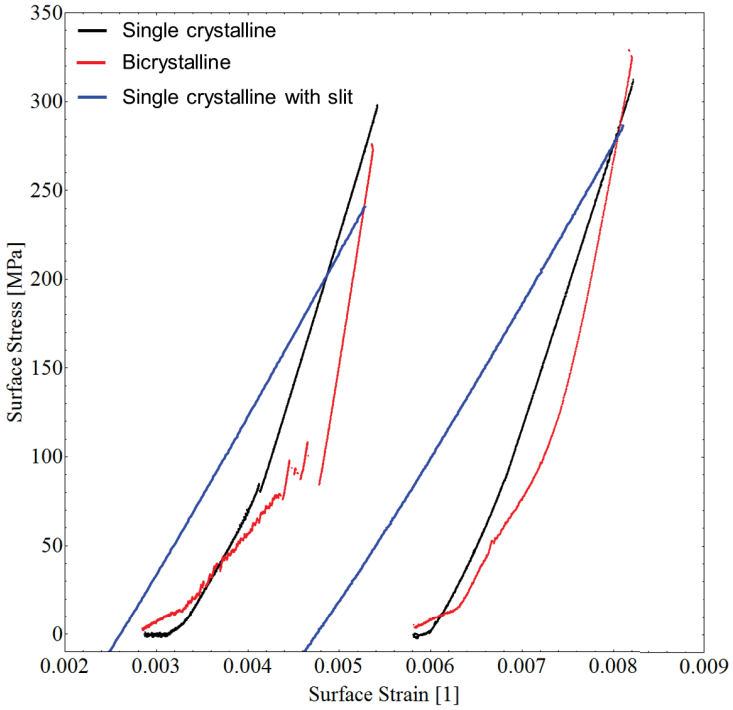


**Figure 4.4** Unloading curves of the *in situ* SEM experiments with the Hysitron indenter at low and high surface strain values of the single crystalline (black), bicrystalline (red) and the single crystalline sample with the slit (blue). An amplification of the single crystalline reverse strain is achieved for the bicrystalline sample, a weakening can be seen for the single crystalline sample with the slit. The effect is decreasing with increasing deformation. Note that the stiffness of the sample base is not corrected here.

# Chapter 5

# Summary and Outlook

The growing market of the microelectronic industry, as well as the demand for micron-sized devices in medical applications require a thorough understanding of material properties in small dimensions. The different material behavior of microscopic samples compared to their macroscopic counterparts are in the focus of materials science for several years now. The benefit of the used *in situ* $\mu$Laue technique is its capability of interlinking mechanical data with dislocation activity, leading to an enhanced understanding of the mechanical behavior at the micron scale.

In the present work *in situ* $\mu$Laue bending tests were performed using bending beams in the dimension of 7x7x21 $\mu m^3$ with three different boundaries at the neutral axis: 1) single crystalline bending beam, 2) bicrystalline bending beam with the grain boundary aligned along the neutral axis, 3) single crystalline bending beam with a slit, cut out along the neutral axis. $\mu$Laue measurements performed by Kirchlechner et al. [14] using sample geometry 1) revealed a reversibility of dislocation pile-ups and consequently a plastic reverse deformation, which was indicated by a nonlinear unloading curve, as well as a reduction in $FWHM_\xi$ observed from the diffraction data. The aim of this work is to clarify the influence of the dislocation pile-up on the nonlinear nature of unloading curves from microbending experiments. Therefore sample geometry 2) was used to amplify and sample geometry 3) to weaken the dislocation pile-up.

The $\mu$Laue measurements using the single crystalline sample showed the expected reversibility of dislocation pile-ups in the stress-strain curves as well as in the $\mu$Laue data in terms of a reduction of 93% of the $FWHM_\xi$ in the first loading step. The bicrystalline sample showed a reverse strain smaller than observed for the single crystalline sample and also the reduction of the $FWHM_\xi$ of 65% in the first unloading step was smaller than for the single crystalline sample, indicating a smaller reversibility of the dislocation pile-up. Thus, the expected

amplified reversibility of the dislocation pile-up was not observed, although SEM images reveal that the grain boundary behaves as an impenetrable barrier. For the single crystalline sample with the slit an almost ideal elastic unloading curve and a marginal reduction of the $FWHM_{\xi}$ was achieved.

Because of an enhanced force resolution compared to the mechanical measurements performed with the straining device at the Synchrotron additional *in situ* SEM experiments were performed with a Hysitron indenter. The obtained stress-strain curves show an amplification of the dislocation pile-up for the bicrystalline sample in terms of a larger reverse deformation compared to the single crystalline sample. The almost ideal elastic unloading behavior of the single crystalline sample with the slit indicated a weakening of the dislocation pile-up. Hardening was observed for the bicrystalline and softening for the single crystalline sample with the slit.

For further experiments it would be interesting to clarify the influence of different orientations, different stacking fault energies and different boundaries on the reversibility of the dislocation pile-up. Different sized bending beams could be used to investigate the existence of a size dependent unloading behavior in microbending tests.

# Chapter 6

# Appendix

## 6.1 Overview of performed experiments

| | Sample | *In situ* Laue | Laue mesh scan | $\sigma$-$\epsilon$ at beamline | $\sigma$-$\epsilon$ at SEM |
|---|---|---|---|---|---|
| **Sxx** | A1 | x | x | x | - |
| **Sxx** | A2 | x | x | x | - |
| **Sxx** | A3 | x | x | x | - |
| **Sxx** | A4 | x | x | x | - |
| **Sxx** | A5 | x | x | x | - |
| **Sxx** | A6 | - | - | - | x |
| **Bxx** | B1 | x | x | - | - |
| **Bxx** | B2 | x | x | x | - |
| **Bxx** | B3 | x | x | x | - |
| **Bxx** | B4 | - | - | - | x |
| **Slit** | C1 | x | x | x | - |
| **Slit** | C2 | x | x | x | - |
| **Slit** | C3 | x | x | x | - |
| **Slit** | C4 | - | - | - | x |

**Table 6.1** The individual experiments performed with each sample are marked with an x.

## 6.2 Glide Step Formation

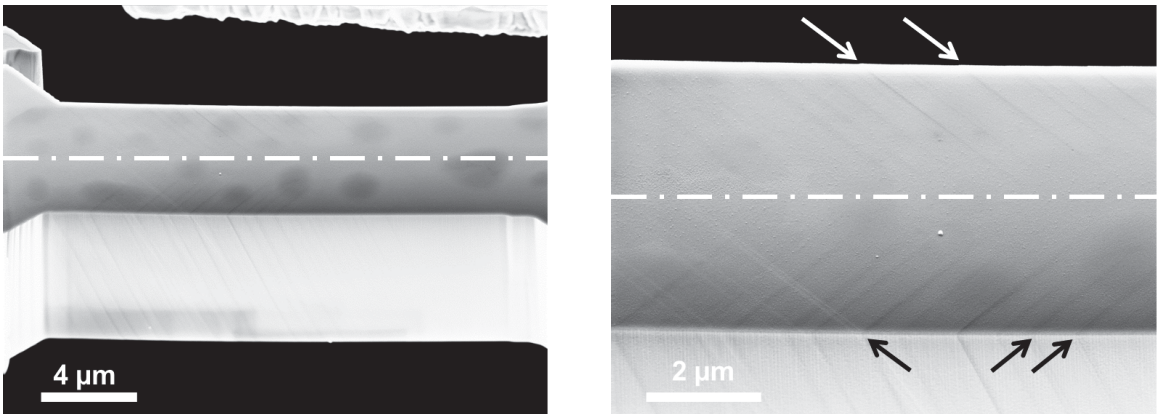


(a) (b)

**Figure 6.1** a) SEM image of the single crystalline sample A5. b) Different oriented glide steps along the tension (black arrows) and compression side (white arrows) can be seen in the larger scaled image.

## 6.3 Laue - Stress-Strain Curve

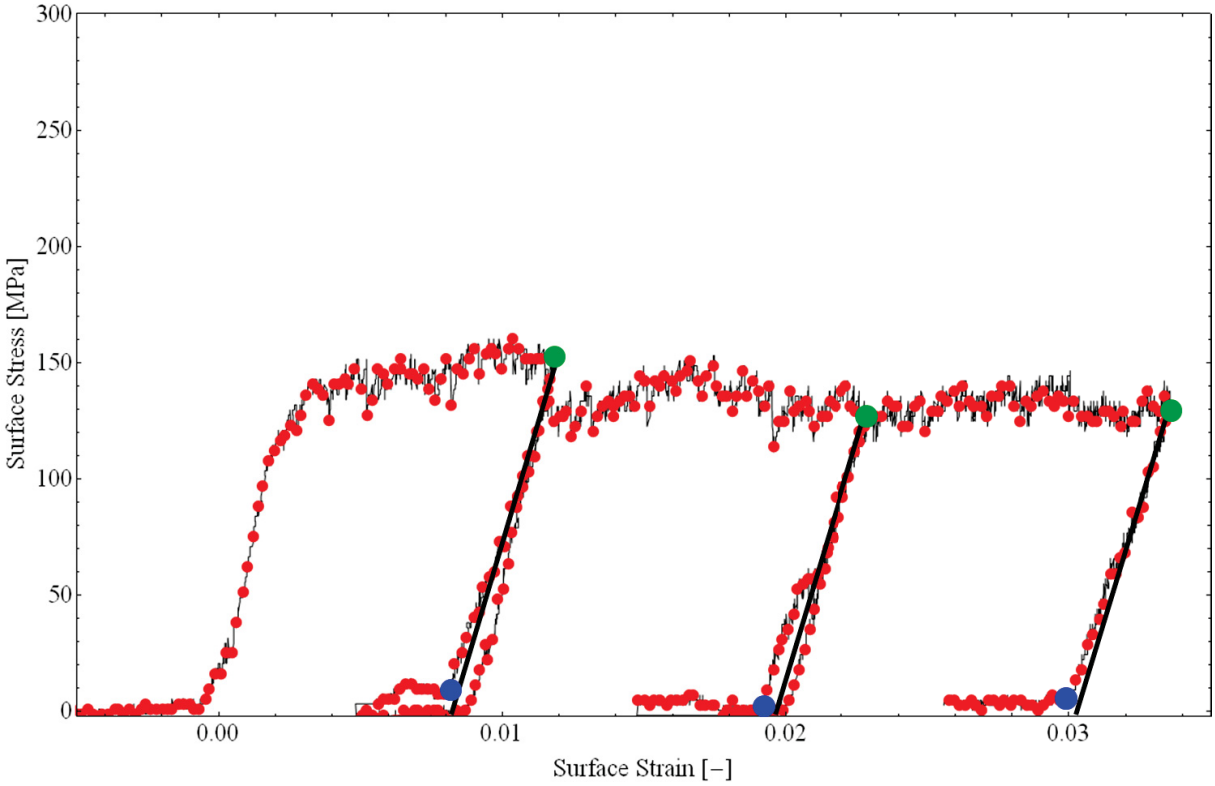


**Figure 6.2** Stress-strain curve of the single crystalline sample C1 with a slit along the neutral axis. The unloading curves are not ideal elastic as expected, which is more pronounced for deformation step two and three.

## 6.4 Maximum Surface Stress

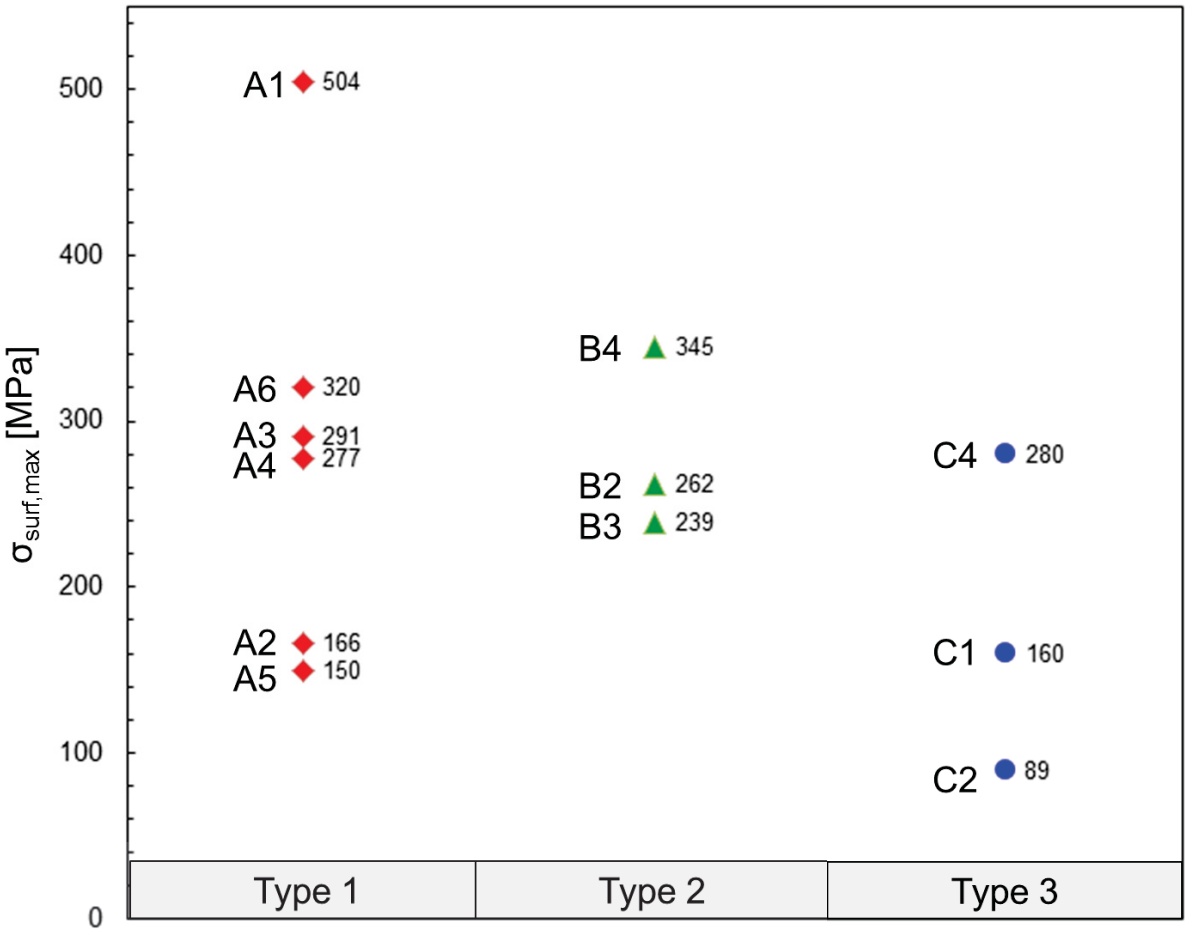


**Figure 6.3** Maximum values of surface stress for the single crystalline samples (type 1), the bicrystalline samples (type 2) and single crystalline samples with the slit (type 3) are considerably scattered.

## 6.5 Shielding from Air Flow

The air flow coming from the air conditioning system was only shielded from the left side of the straining device in former *in situ* $\mu$Laue experiments (Fig. 6.4a). A recently installed canvas covering in the top of the straining device redirected the air flow in such a way, that an allover shielding was necessary to prevent an impact on the tungsten wire of the load cell in the straining device 6.4b. The missing allover covering for sample number B1 is the reason for its unavailable stress-strain curve.

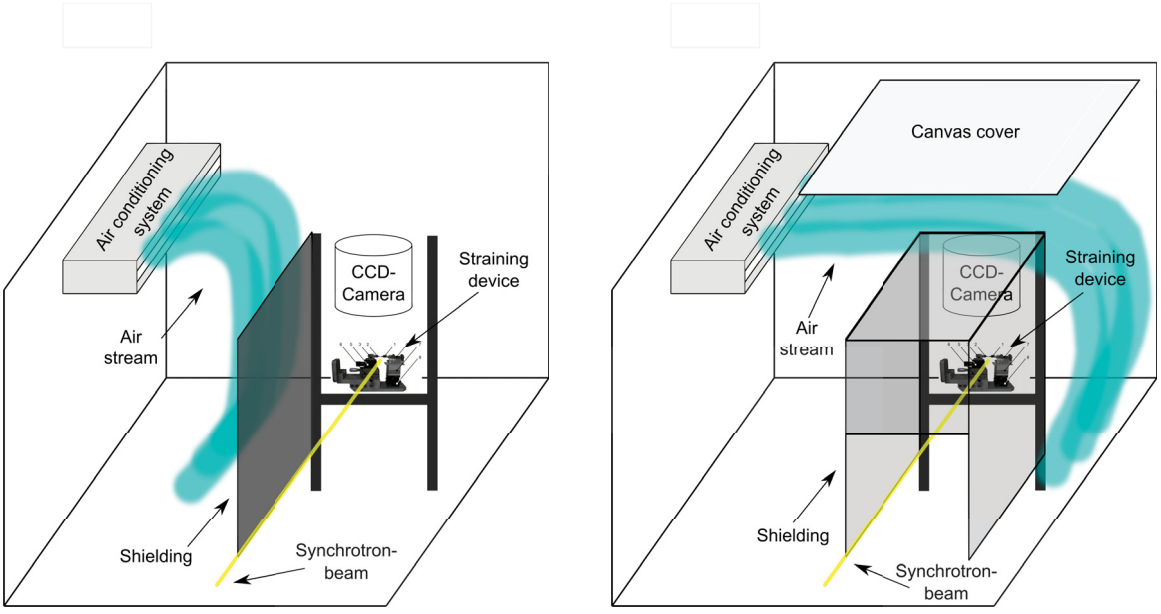


(a) (b)

**Figure 6.4** a) The air flow in former *in situ* $\mu$Laue experiments had only to be shielded from the left side of the straining device. b) A recently installed canvas covering led to a redirected air flow. The allover shielding served to protect the tungsten wire of the load cell from the impact of the air flow.

# List of Figures

# List of Tables

# Bibliography

[1] G. Dehm. Miniaturized single-crystalline fcc metals deformed in tension: New insights in size-dependent plasticity. *Progress in Materials Science*, 54:664–688, 2009.

[2] D. Kiener, W. Grosinger, G. Dehm, and R. Pippan. A further step towards an understanding of size-dependent crystal plasticity: In situ tension experiments of miniaturized single-crystal copper samples. *Acta Materialia*, 56:580–592, 2008.

[3] M.D. Uchic, D.M. Dimiduk, J.N. Florando, and W.D. Nix. Sample dimensions influence strength and crystal plasticity. *Science*, 305:986–989, 2004.

[4] C. A. Volkert and E. T. Lilleodden. Size effects in the deformation of sub-micron au columns. *Philosophical Magazine*, 86:5567–5579, 2006.

[5] J.S. Stölken and A.G. Evans. A microbend test method for measuring the plasticity length scale. *Acta Materialia*, 46(14):5109–5115, 1998.

[6] R. Pippan C. Motz, T. Schöberl. Mechanical properties of micro-sized copper bending beams machined by the focused ion beam technique. *Acta Materialia*, 53:4269–4279, 2005.

[7] E. Demir and D. Raabe. Mechanical and microstructural single-crystal bauschinger effects: Observation of reversible plasticity in copper during bending. *Acta Materialia*, 58:6055–6063, 2010.

[8] J. Gong and A. Wilkinson. Micro-cantilever testing of a prismatic slip in commercially pure ti. *Philosophical Magazine*, 59:5970–5981, 2010.

[9] C. Motz, D. Weygand, J. Senger, and P. Gumbsch. Micro-bending tests: A comparison

between three-dimensional discrete dislocation dynamics simulations and experiments. *Acta Materialia*, 56:1942–1955, 2008.

[10] M. von Ardenne, G. Musiol, and U. Klemradt. *Effekte der Physik und ihre Anwendungen*. 2005.

[11] T. Hasegawa, T. Yakou, and U.F. Kocks. Forward and reverse rearrangements of dislocations in tangled walls. *Material Science and Engineering*, 81:189–199, 1986.

[12] F. Mompiou, D. Caillard, M. Legros, and H. Mughrabi. In situ tem observations of reverse dislocation motion upon unloading in tensile-deformed ufg aluminium. *Acta Materialia*, 60(8):3402–3414, 2012.

[13] H.W. Höppel, M. Kautz, C. Xu, M. Murashkin, T.G. Langdon, R.Z. Valiev, and H. Mughrabi. An overview: Fatigue behaviour of ultrafine-grained metals and alloys. *International Journal of Fatigue*, 28:1001–1010, 2006.

[14] C. Kirchlechner, W. Grosinger, M.W. Kapp, P.J. Imrich, J.S. Micha, O. Ulrich, J. Keckes, G. Dehm, and C. Motz. Investigation of reversible plasticity in a micron sized, single crystalline copper bending beam by x-ray $\mu$laue diffraction. *Philosophical Magazine*, -:1–12, 2012.

[15] C. Kirchlechner, D. Kiener, C. Motz, S. Labat, N. Vaxelaire, O. Perroud, J.S. Micha, O. Ulrich, O. Thomas, G. Dehm, and J. Keckes. Dislocation storage in single slip oriented cu micro-tensile samples: New insights by x-ray microdiffraction. *Philosophical Magazine*, 91:1256–1264, 2011.

[16] C. Kirchlechner, J. Keckes, C. Motz, W. Grosinger, M.W. Kapp, J.S. Micha, O. Ulrich, and G. Dehm. Impact of instrumental constraints and imperfections on the dislocation structure in micron-sized cu compression pillars. *Acta Materialia*, 59:5618–5626, 2011.

[17] C. Kirchlechner, J. Keckes, J.S. Micha, and G. Dehm. In situ $\mu$laue: Instrumental setup for the deformation of micron sized samples. *Adv. Eng. Mater.*, 13:837–844, 2011.

[18] C. Kirchlechner, P.J. Imrich, W. Grosinger, M.W. Kapp, J. Keckes, J.S. Micha, O. Ulrich, O. Thomas, S. Labat, C. Motz, and G. Dehm. Expected and unexpected plastic behavior at the micron scale: An in situ $\mu$laue tensile study. *Acta Materialia*, 60:1252–1258, 2012.

[19] R.I. Barabash, G.E. Ice, B.C. Larson, G.M. Pharr, K.-S. Chung, and W. Yang. White microbeam diffraction from distorted crystals. *Appl. Phys. Lett.*, 79:749–751, 2001.

[20] G. Ice and R.I. Barabash. *White Beam Microdiffraction and Dislocations Gradients*, chapter 79, pages 502–598. Elsevier B.V., 2007.

[21] G. Ice and J.W.L. Pang. Tutorial on x-ray microlaue diffraction. *Mater. Charact.*, 60:1191–1201, 2009.

[22] G. Moser, H. Felber, B. Rashkova, P.J. Imrich, C. Kirchlechner, W. Grosinger, C. Motz, G. Dehm, and D. Kiener. Sample preparation by metallography and focussed ion beam for nanomechanical testing. *Pract. Metallogr.*, 49:1–13, 2012.

[23] L.A. Giannuzzi and F.A. Stevie. *Introduction To Focused Ion Beams: Instrumentation, Theory, Techniques and Practice*. Springer, 2005.

[24] C.A. Volkert and A.M. Minor. Focused ion beam microscopy and micromachining. *MRS Bulletin*, 32:389–399, 2007.

[25] M. von Laue. Concerning the detection of x-ray interferences. *Nobel Lecture*, -:347–355, 1915.

[26] L. Spieß, R. Schwarzer, H. Behnken, and G. Teichert. *Moderne Röntgenbeugung*. Vieweg und Teubner, 2009.

[27] C. Kirchlechner. *Plasticity at the Micron Scale: A μLaue Study*. PhD thesis, University of Leoben, 2011.

[28] W. Pantleon. Resolving the geometrically necessary dislocation content by conventional electron backscattering diffraction. *Scripta Materialia*, 58:994 – 997, 2008.

[29] G. Gottstein. *Physikalische Grundlagen der Materialkunde*. Springer, 2001.

[30] G. Margaritondo. *Introduction to Synchrotron Radiation*. Oxford University Press, 1988.

[31] O. Ulrich, X. Biquard, P. Bleuet, O. Geaymond, P. Gergaud, J. S. Micha, O. Robach, and F. Rieutord. A new white beam x-ray microdiffraction setup on the bm32 beamline at the european synchrotron radiation facility. *Review of Scientific Instruments*, 82:–, 2011.

[32] R. Ghisleni, K. Rzepiejewska-Malyska, L. Philippe, P. Schwaller, and J. Michler. In situ sem indentation experiments: Instruments, methodology, and applications. *Microscopy Research and Technique*, 72:242–249, 2009.

[33] J. D. Nowak, K.A. Rzepiejewska-Malyska, R. C. Major, O.L. Warren, and J. Michler. In-situ nanoindentation in the sem. *Materials Today*, 12:44–45, 2009.

[34] Hysitron Inc. *Tribo Analysis User Manual*. 2009.

[35] D. Kiener, C. Motz, W. Grosinger, D. Weygand, and R. Pippan. Cyclic response of copper single crystal micro-beams. *Scripta Materialia*, 63:500–503, 2010.